Journal of Colloid and Interface Science 696 (2025) 137873

Contents lists available at ScienceDirect

Journal of Colloid And Interface Science

journal homepage: www.elsevier.com/locate/jcis

Regular Article

Biofriendly glucose-derived carbon nanodots: GLUT2-mediated cell internalization for an efficient targeted drug delivery and light-triggered cancer cell damage

Nicolo Musso [a,b,*,1], Paolo Giuseppe Bonacci [b,1], Grazia Maria Letizia Consoli [c,1], Ludovica Maugeri [d], Morena Terrana [b], Luca Lanzanò [e], Elisa Longo [e], Gianpiero Buscarino [f], Antonino Consoli [g], Salvatore Petralia [c,d,*]

[a] Faculty of Medicine and Surgery, "Kore" University of Enna, Contrada Santa Panasia, 94100 Enna, Italy
[b] Department of Biomedicals and Biotechnologies Sciences, University of Catania, Via S. Sofia 97, 95123 Catania, Italy
[c] CNR-Institute of Biomolecular Chemistry, Via Paolo Gaifami 18, 95126 Catania, Italy
[d] Department of Drug and Health Sciences, University of Catania, Via Santa Sofia 64, 95125 Catania, Italy
[e] Department of Physic and Astronomy, University of Catania, Via Santa Sofia 64, 95125 Catania, Italy
[f] Department of Physics and Chemistry, University of Palermo, Via Archirafi 36, 90123 Palermo, Italy
[g] Department of Chemical, Biological, Pharmaceutical and Environmental Sciences, University of Messina, Viale Ferdinando Stagno d'Alcontres 31, 98166 Messina, Italy

GRAPHICAL ABSTRACT

Emissive and photothermal glucose-based carbon nanodots were prepared by a green one-pot mild thermal process from glucose precursor. The outer glucose shell exhibited biofriendly and water dispersible properties. The targeted drug delivery and photothermal cell damage activities mainly driven by GLUT2 transporter were demonstrated.

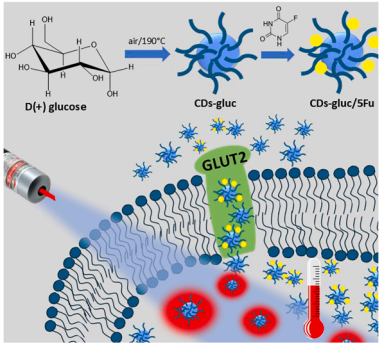

* Corresponding authors at: Faculty of Medicine and Surgery, "Kore" University of Enna, Contrada Santa Panasia, 94100 Enna, Italy (Nicolo Musso). Department of Drug and Health Sciences, University of Catania, Via Santa Sofia 64, 95125 Catania, Italy (Salvatore Petralia).
E-mail addresses: nmusso@unict.it (N. Musso), salvatore.petralia@unict.it (S. Petralia).
[1] These authors equally contributed.

https://doi.org/10.1016/j.jcis.2025.137873
Received 4 April 2025; Received in revised form 9 May 2025; Accepted 11 May 2025
Available online 15 May 2025
0021-9797/© 2025 The Author(s). Published by Elsevier Inc. This is an open access article under the CC BY license (http://creativecommons.org/licenses/by/4.0/).

ARTICLE INFO

Keywords:
Carbon-nanodots
Cellular internalization
Nanomaterials
Photothermal effect
Photoluminescence
Glucose transporter

ABSTRACT

Personalized medicine holds great promise for treating the underlying causes of many human diseases with high precision. Low-dimensional carbon-based materials are being designed to more closely match specific delivery efficiency for targeted cancer treatment, while enabling the benefits of increased biocompatibility, high cargo-loading capacity and excellent light-responsive properties, including photoluminescence and photothermal effects. Here, we report an unprecedented example of glucose-based carbon-nanodots (CDs-gluc) obtained via a one-pot thermal process from glucose, without using organic solvent and additional reagents. The CDs-gluc nanostructures, composed of a C-sp2 inner core and a glucose outer shell, showed a high photothermal conversion efficiency (η = 42.7 % at 532 nm), good photoluminescence quantum yield (ϕ_{PL} = 6 %), and low cytotoxicity. Measurements of cellular Zeta-potential demonstrated the effective interaction of CDs-gluc with the surface of cancer cells overexpressing the Glucose Transporter Type 2 (GLUT2). The effective and specific GLUT2-mediated internalization mechanism was demonstrated by inducing up- and down-regulation of the transporter expression under conditions of glucose excess and deprivation, through fluorescence correlation spectroscopy. The potential of the CDs-gluc as drug nanocarriers was demonstrated by entrapping the anticancer drug 5-fluorouracil, achieving a drug loading capacity of 4.5 ± 0.8 %. In vitro experiments confirmed the excellent light-triggered cell damage activity and remarkable cell-targeting ability of CDs-gluc driven by GLUT2 expression. The easy and green preparation, biocompatibility, effective and specific cellular uptake, photoluminescence and hyperthermia make CDs-gluc appealing candidates in the research of novel nanostructures for cancer cell targeting.

1. Introduction

Low-dimensional materials represent an intriguing category of nanostructures, offering a multitude of advantageous characteristics, including high surface area, a diverse range of surface chemistries, precisely controllable structures, and unique optical and physical properties [1,2].

A broad array of carbon-, metal-, graphitic carbon nitride-, metal oxide-, and boronnitride-derived nanomaterials with distinctive chemical, optical, and stimuli responsive characteristics have been developed [3–7].

Nanoparticles, nanodots and quantum dots, that were recently awarded the 2023 Nobel Prize in Chemistry, can respond to a variety of external stimuli, including pH, temperature, light, and magnetism. This responsiveness, combined with (i) their ability to deliver and co-deliver therapeutic [8], diagnostic and theranostic agents, (ii) the possibility of surface functionalizationwith ligands (e.g., carbohydrates, choline, transferrin, folic acid, antibodies, peptides, aptamers) that recognize transporters overexpressed on tumor cells, and (iii) their intrinsic luminescence and photoresponsive properties, makes these nanostructures highly promising smart agents for more effective, safer, and personalized cancer treatments [9]. Smart nanosystems thanks to their nanoscale size can preferentially accumulate in tumor tissue through the Enhanced Permeability and Retention (EPR) effect, while binding specific receptors can target cancer cells while sparing normal cells [10,11]. Smart nanosystems through a controlled drug release, [11,12] also triggerable by external stimuli such as acidic pH of cancer cells or local light irradiation, can prolong drug circulation time and minimize systemic toxicity and undesired side effects [13]. Nanosystems can also perform a more effective cancer cell attack through the simultaneous delivery of diverse drugs (multidrug therapy) or through a combined chemo-photothermal effect (combination therapy) [14].

A comprehensive analysis of specific transporters expressed on cancer cell surface is essential for the development of an effective targeted cancer treatment. Among membrane transporters, Glucose Transporters (GLUTs) play a pivotal role in tumor growth due to their involvement in the Warburg effect, whereby cancer cells metabolize glucose at a higher rate than normal cells [15–18]. GLUTs facilitate glucose uptake, supplying energy and nutrients necessary for cancer cell survival and proliferation. Upregulation of GLUT expression ensures a continuous supply of glucose [19], thus promoting cell growth even in hypoxic microenvironments typical of tumors [20]. High expression of GLUT isoforms has been linked to multiple facets of tumor progression, including augmented proliferation, apoptosis resistance, and metastasis [21,22]. Therefore, inhibition of GLUT transporters or their use for cancer cell recognition and penetration, as well as interference with glucose metabolism pathways, have been identified as potential strategies to target cancer cells, while simultaneously minimizing damage to healthy cells expressing GLUT at lower levels [23–25]. Among the GLUT family, GLUT2 (Glucose Transporter Type 2) [26] is predominantly located in liver, pancreas, kidney, and small intestine cells (Scheme 1A) [27]. GLUT2 exhibits low affinity for glucose but high transport capacity, making it critical in tissues requiring substantial amounts of glucose. Recent studies have indicated that GLUT2 may be overexpressed in certain cancer cells, including colon and breast cells [28,29]. Recently, Kin and coworker proposed glucosamine-based photoluminescent carbon nanodots as targeting probes for diagnosing hepatocellular carcinoma by specific GLUT2 binding [30]. Their in vitro experiments confirmed the probe specificity by testing on GLUT2-modified cells.

Here, we report the synthesis, characterization, and GLUT2-mediated internalization of glucose-derived carbon nanodots (CDs-gluc). CDs-gluc were synthesized through a one-step thermal process from D(+)glucose as the unique precursor, without solvents or additional reagents (Scheme 1B). Parameters as optical properties, including luminescence, photothermal effect and capacity to produce reducing electrons (e^-) or oxidizing holes (h^+) upon blue-light excitation (Scheme 1C), have been investigated to assess the potential of CDs-gluc as a light-actuated intriguing material for remote-controlled hyperthermia, bioimaging, photooxidation and photoreduction applications. To the best of our knowledge, for the first time GLUT2-mediated cell uptake of glucose-derived carbon-dots has been investigated by modulating GLUT2 expression level across six different cell lines. The interaction between CDs-gluc and GLUT2 overexpressing cells was also demonstrated by Z-potential measurements, while cellular uptake was confirmed by blue luminescence imaging. In vitro experiments demonstrated efficient and selective cancer cell targeting using 5fluorouracil (5Fu)-loaded CDs-gluc and light-triggered cell damage activity of CDs-gluc driven by GLUT2 expression (Scheme 1D).

2. Result and discussion

2.1. CDs-gluc synthesis and characterization

Glucose-based carbon-nanodots (CDs-gluc) were prepared from D(+) glucose using an innovative one-pot method recently developed in our laboratory [31]. Heating the glucose precursor at 190 °C in air for 45 min led to the formation of CDs-gluc, as illustrated in Scheme 1B. The thermal reaction was conducted without the use of solvents, oxidizing

agents, or acids, and without the use of equipment such as microwaves or autoclaves, commonly used for the preparation of similar carbon-nanodots [32]. The as-prepared CDs-gluc consist of an inner Csp^2 carbon core and an outer glucose shell.

The UV − vis optical absorption spectra of CDs-gluc displayed typical absorption bands for carbon-nanodots. In particular, the spectra showed a band at around 281 nm corresponding to the ππ* transition ($\varepsilon_{\pi\pi^*} = 1.99 \pm 0.3\ cm^{-1}\ g^{-1}\ L$) associated with aromatic carbon-sp^2 and a lower and broad band at around 360 nm, relating to the nπ* transition generated by C═C and C═O bonds (Fig. 1A). The optical band gap was calculated from the Tauc's plot, which showed the variation of $(Ass\ h\upsilon)^{1/2}$ *versus* ($h\upsilon$) for CDs-gluc (inset Fig. 1A). The optical energy band gaps (E_g) for the allowed transitions were estimated to be about $Eg_1 = 2.0$ eV and $Eg_2 = 3.4$ eV. These values are in good agreement with similar carbonaceous nanodots reported in the literature [33].

Fig. 1B depicts the emission spectrum of CDs-gluc in water at various excitation wavelengths from 360 to 520 nm. The emission decreases with increasing the excitation wavelength, clearly evidencing the excitation-dependent photoluminescence behavior typical of carbon-based nanodots. The photoluminescence quantum yield (ϕ_{PL}) of CDs-gluc in water was calculated to be about 6 %. This value is consistent with the data reported by Piasek and colleagues [34]. They have investigated the fluorescence efficiency of glucose-derived carbon dots synthesized by microwave method and demonstrated that the fluorescence efficiency depends on a number of process parameters, including time and temperature of reaction, which in turn influence the size and aggregation of the nanostructure. The authors confirmed that higher fluorescence is favored by longer heating time at 200 °C, according to a more extensive carbonization process. Recently, Kang and coworkers developed a facile method for the preparation of carbon nanodots from glucose via an aldol reaction, and interestingly showed that the resulting CDs retained the chiral properties of the glucose precursor [35].

The effective formation of CDs-gluc was supported by infrared spectroscopy ATR-FTIR (Fig. 1C), showing the following diagnostic peaks for glucose: 3410–3258 cm^{-1} (O—H, stretching), 2916 cm^{-1} (C—H, stretching), 1146–960 cm^{-1}(C—O, stretching) and a signal at 1655 cm^{-1} (C═O, stretching) correlated to the carboxylic groups within the carbon core structure. For comparison, Fig. 1C also displays the spectrum of the glucose precursor, with peaks at 3403–3196 cm^{-1} (O—H, stretching), 2947–2890 cm^{-1} (C—H, stretching), 1332 cm^{-1} (C—C bending), 1142 cm^{-1} (C—O, stretching), 1109 cm^{-1} (C—O—C, stretching), 1047–976 cm^{-1} (C—O, stretching), 988–700 cm^{-1} (vibration of pyranose ring).

Solution-state nuclear magnetic resonance spectroscopy (NMR) is a technique used to gain information on the shell structure covering the carbonaceous core of CDs, including glucose-derived CDs [35–37]. The ^1H- and ^{13}C NMR spectra of CDs-gluc evidenced the presence of a glucose shell. They showed signals in the range 3–6 ppm and 60–110 ppm, typical for glucose (Fig. 1D-E). Purification of the sample by dialysis ruled out that these signals are due to free glucose in solution. Multiple signals for the glucose moieties, particularly evident in the anomeric group region and in the 2D-COSY-NMR spectrum (Fig. S1) due to overlapping signals, suggested a shell with glucose units in various conformations, including α- and β-pyranose anomers. A furanose-like conformation, possibly resultingfrom the dehydration during the thermal treatment, could also be present [38,39]. The evident downfield shift of the anomeric signals in the carbon spectrum of CDs-gluc compared to the glucose precursor (Fig. 1E) further indicated the involvement of anomeric groups in covalent bonds.

Notably, differently from other glucose-derived CDs [35–37], the NMR spectra of CDs-gluc showed very small proton signals in the 1–3 ppm range and no detectable carbon signals in the 20–35 ppm and

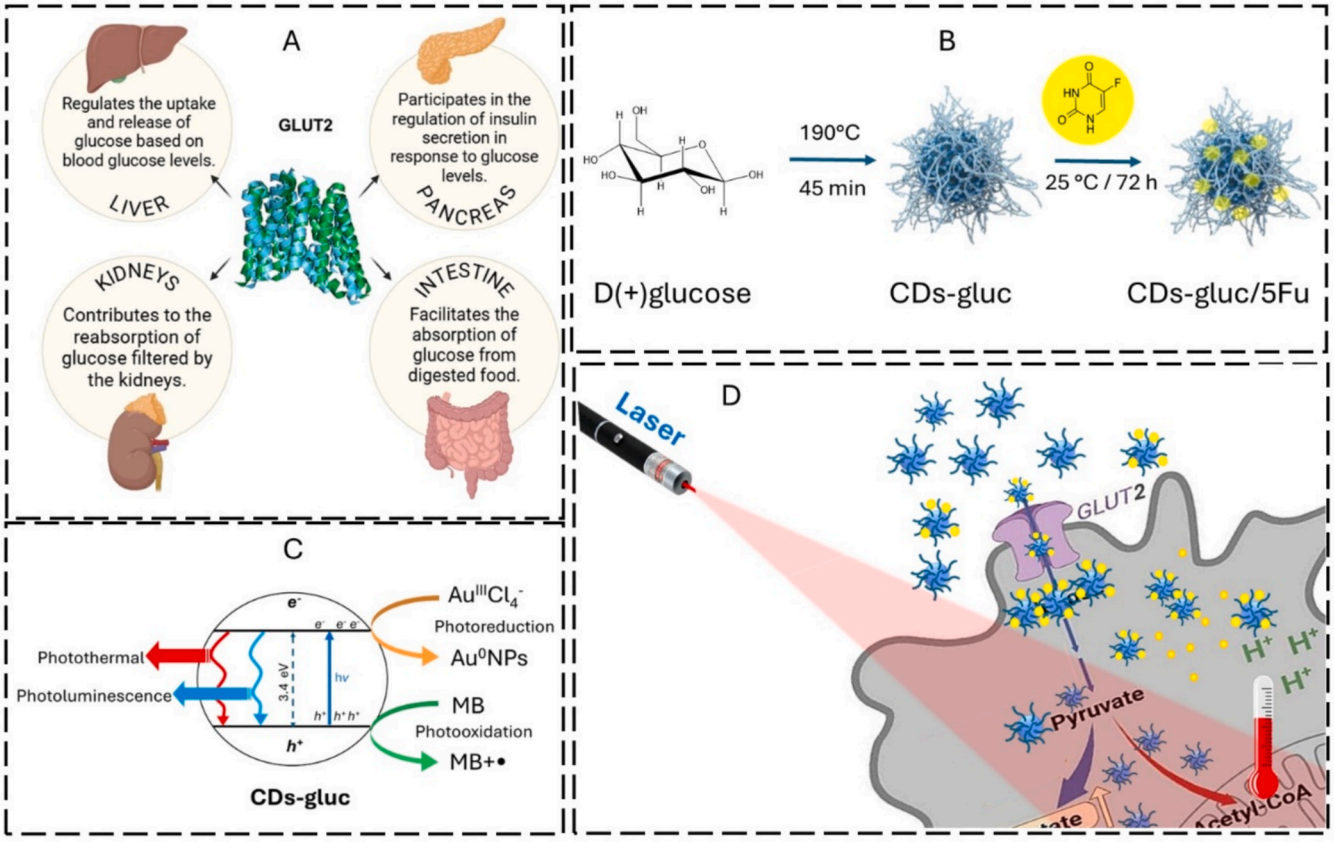

Scheme 1. CDs-gluc: A) Role of GLUT2 in different tissues, B) schematic chemical procedure for the synthesis of CDs-gluc and CDs-gluc/5Fu, C) photophysical properties of CDs-gluc, and D) GLUT2-mediated cellular internalization mechanism for cell damage activities triggered by light and/or drug delivery.

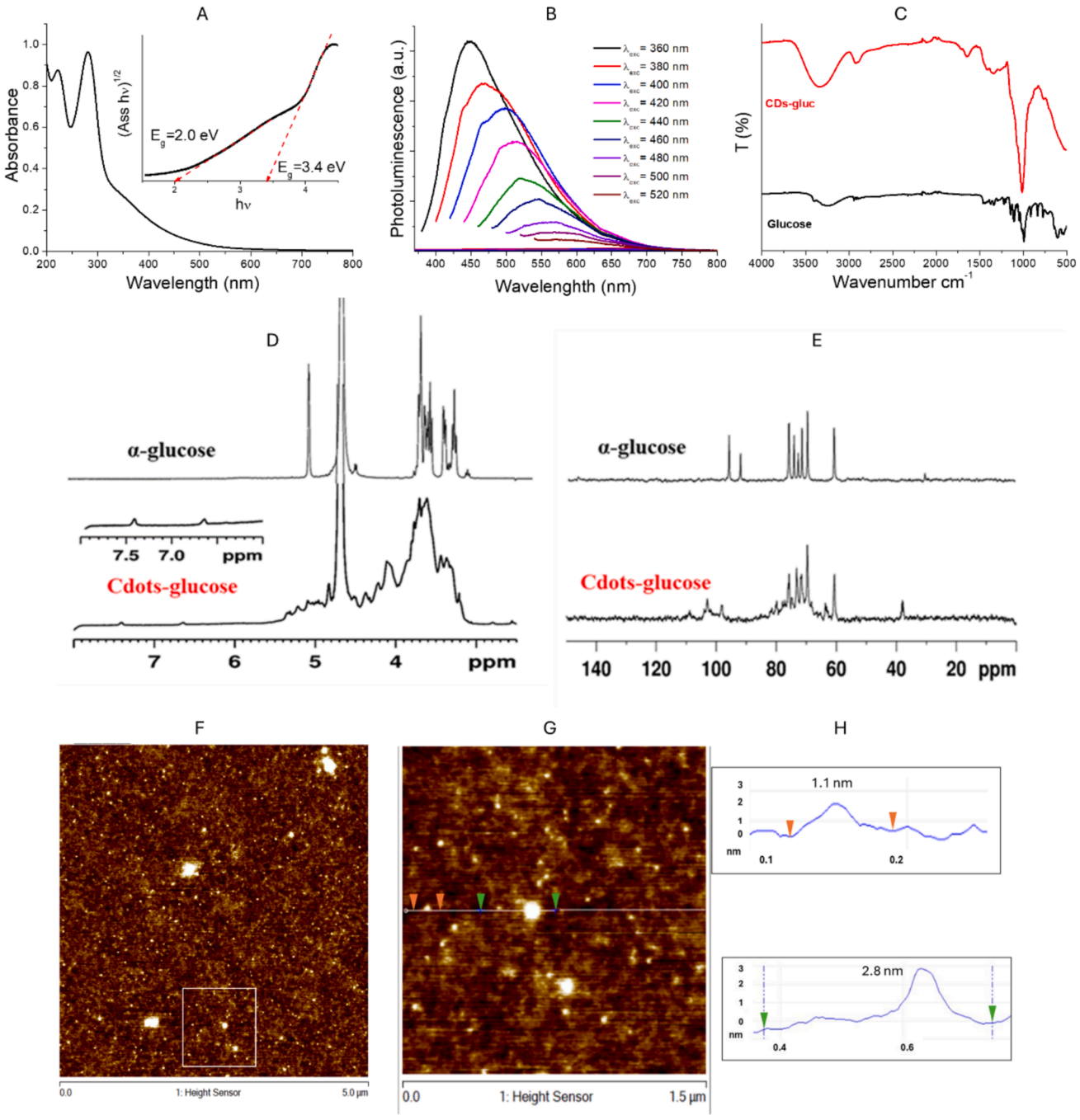

Fig. 1. CDs-gluc characterization: A) optical absorption spectrum of CDs-gluc dispersions in water (0.55 mg mL^{-1}), inset the Tauc's plot for the optical band gap evaluation, B) fluorescence spectrum in water at various excitation wavelengths, C) ATR-FTIR spectra of CDs-gluc (red line) and glucose precursor (black line), D) ^{1}H NMR spectra of CDs-gluc and glucose precursor in D_2O at 297 K; E) ^{13}C NMR spectra of CDs-gluc and glucose precursor in D_2O at 297 K, F) AFM image full scan size 5 × 5 µm; G) AFM image full scan size 1.5 × 1.5 µm, and H) cross section profiles of CDs-gluc.

165–180 ppm range, which are characteristic of aliphatic sp^3 CH and CHO groups (Fig. S2). This suggested that the optimized synthesis (glucose heating at mild temperature for 45 min) produces a negligible amount of oxidized non-cyclic by-compounds derived from the aperture of the glucose ring. In contrast, significant oxidation, dependent on temperature and reaction time, was reported for glucose-derived CDs synthetized by microwave method. Their NMR spectra showed the disappearance of glucose signals and indicated the presence of a polymeric shell composed of butyric acid and/or butanal surrounding a carbon core [35]. Similar to other glucose-derived CDs, it is plausible that the formation of CDs-gluc by mild heating involves reticulation reactions (dehydration and polymerization) of the sugar moieties followed by carbonization. Generally, the core of CDs are invisible in liquid-state NMR due to limited mobility of the rigid structure; however, in the proton spectrum of CDs-gluc were visible two small signals at 6.5 and 7.4 ppm (Fig. S2) that along with the UV–Vis absorption peak at 281 nm (Fig. 1A), support the presence of an aromatic core in the structure. A small signal at 9.40 ppm can be attributed to the presence of carboxylic groups in the nanostructure.

According to the bottom-up approach, using relatively gentle methods and short reaction times limited carbonization occurs and CDs with a small core are formed. A small core surrounded by a glucose shell

agrees with the high water solubility and stability of the CDs dispersion, which showed no significant changes in the NMR spectra even months after their preparation.

The morphology and size of CDs-gluc were investigated by contact-mode Atomic Force microscopy (AFM). Fig. 1F–H show representative full scan 5 × 5 μm and 1.5 × 1.5 μm AFM images. Fig. 1G shows profile sections of CDs-gluc with heights of about 1.1 and 2.8 nm. The AFM investigation revealed the presence of spherical-shaped CDs-gluc nanostructures with a 0.2–2.0 nm height distribution range and few larger particles in the 2.4–3.4 nm range. A height distribution histogram, obtained by analysis of multiple AFM images, is shown in Fig. S3. Additional AFM images (1.1 × 1.1 μm) and cross-section profiles of CDs-gluc, reported in Fig. S4, confirmed the presence of small (0.9 nm) and larger (4.1 nm) nanostructures.

2.2. CDs-gluc photophysical properties

CDs-gluc exhibited interesting photophysical properties as photocatalytic and photothermal effects upon blue light excitation. In particular, upon absorption of UV-photons (300–400 nm), the carbon-sp^2 core of the nanostructures produces solvated electrons (e^-) and holes (h^+) through reaction (1), thereby inducing photooxidation and photoreduction processes.

$$\text{CDs-gluc} + h\upsilon(300\ \text{nm}) \rightarrow \text{CDs-gluc}(h^+) + \text{solv-}e^- \quad (1)$$

The photooxidant properties of CDs-gluc were spectroscopically confirmed by using methylene blue (MB) as h^+ scavenger, through reaction (2).

$$\text{MB} + \text{CDs-gluc}(h^+) \rightarrow \text{CDs-gluc} + \text{MB}^{+\bullet} \quad (2)$$

Fig. 2A illustrates the optical absorption spectra of the CDs-gluc/MB dispersion after UV-light irradiation (300 nm) under deaerated conditions and at different time intervals (10, 20, 30, 40, and 50 min). Decreases in the MB absorption band at around 665 nm confirmed the photodegradation of MB. A control experiment conducted under aerated conditions demonstrated that, in the presence of O_2 species, MB photodegradation does not occur (Fig. S5) due to photo-quenching of O_2. The photoinduced oxidation was confirmed by additional experiments conducted under dark conditions. In this case no MB photodegradation was observed (Fig. S5). Fig. 2B summarizes the MB photodegradation (%) under aerated, deaerated, and dark conditions. It is known that upon photoexcitation with UV-photons (300 nm) in the absence of oxygen, reaction (2) is dominant.

The photoreduction properties of CDs-gluc were investigated through the photochemical production of gold nanoparticles ($Au^{(0)}$NPs) by reactions 3 and 4:

$$\text{CDs-gluc} + h\upsilon(300\ \text{nm}) \rightarrow \text{CDs-gluc}(h^+) + \text{solv-}e^- \quad (3)$$

$$Au^{III}Cl_4^- + 3e^- + \text{n CDs-gluc} \rightarrow \rightarrow \text{CDs-gluc/}Au^0\text{NPs} + 4Cl^- \quad (4)$$

In detail, the photogenerated electron (solv-e^-) promote the reduction of Au^{III} to Au^0, while Cds-gluc acts as capping agent, stabilizing the resulting CDs-gluc/Au^0 nanoparticles. Fig. 2C illustrates the optical absorption spectra of the CDs-gluc/$AuCl_4^-$ dispersion after exposure to UV-light irradiation (2 lamps, 300 nm) at various time intervals (0, 2, 4, 6, 8, 10, 15, 20, 25, and 30 min) under deareated conditions. Under these conditions, UV-photons are exclusively absorbed by the CDs-gluc nanostructures. The appearance of the localized surface plasmon resonance (LSPR) band, typical of AuNPs, centered at about 552 nm confirmed the effective photoreduction of the Au^{III} chloride precursor to Au^0 nanostructures. Furthermore, the photochemical process was confirmed by experiments performed under dark conditions, in this case no formation of Au^0 nanostructures was observed (Fig. S6). The inset in Fig. 2C reports the absorbance values at 552 nm for both UV-irradiated () and dark conditions at various irradiation times.

To investigate the photothermal properties of CDs-gluc, an aqueous dispersion (5 mg ml^{-1}, 100 μL, Abs_{405nm} = 1.33) was continuously exposed to a 405 nm laser source. Temperature changes were monitored using a standard thermal-camera. Fig. 2D illustrates representative photothermal cycles of the CDs-gluc dispersion during photothermal experiments using different laser powers. When the system reached its maximum temperature (T_{max}), the laser was switched off, and the

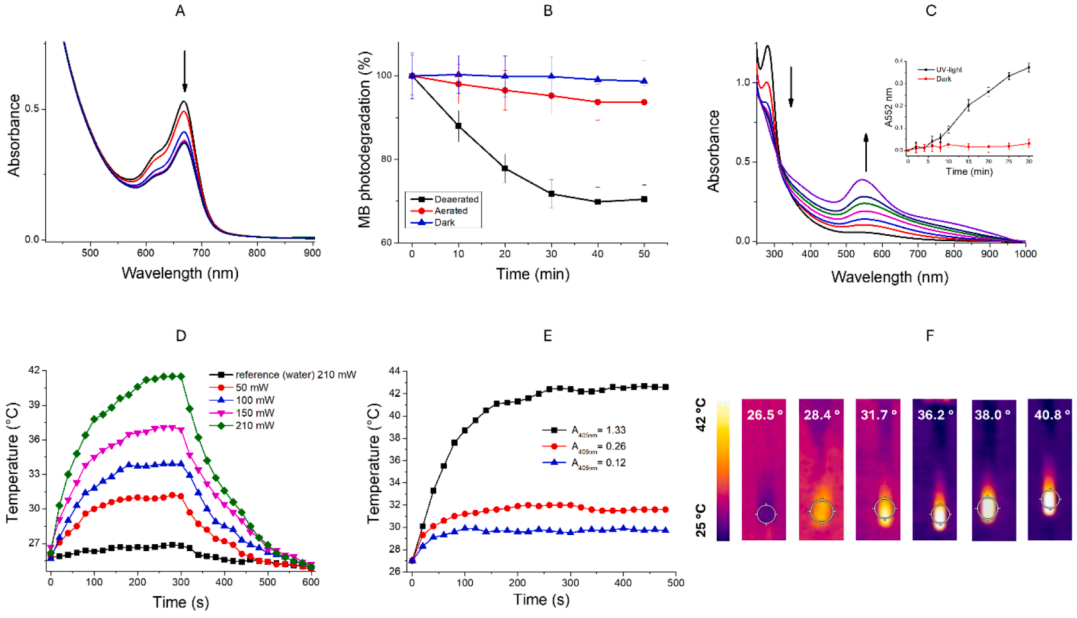

Fig. 2. CDs-gluc photophysical properties. Photo-oxidation experiments of CDs-gluc (5 mg ml^{-1}) water dispersion in the presence of MB upon UV-light irradiation (10, 20, 30, 40, and 50 min, 2 lamps 300 nm): A) optical absorption spectra in the region 420–900 nm of CDs-gluc/MB dispersion and B) MB photodegradation (%) under aerated, deaerated and dark conditions. C) Photoreduction experiments of CDs-gluc, formation of $Au^{(0)}$NPs upon UV-light (300 nm) irradiation at different irradiation times, inserted the absorbance value at 552 nm upon irradiation and dark conditions. D) Photothermal experiments for CDs-gluc aqueous dispersion (5 mg mL^{-1}, 100 μL, Abs_{405nm} = 1.33) at different laser powers 50, 100, 150, and 210 mW, E) different CDs-gluc amount (Laser Power 210 mW), and F) representative thermo-graph during the photothermal experiments.

temperature dropped to the environmental temperature (T_{env}). The power-dependent behavior was confirmed by experiments performed with different laser powers (50, 100, 150, and, 210 mW), and the maximum temperature recorded values were about 31.2, 33.9, 37.1, and 41.6 °C, respectively (Fig. 2D). The T_{env} during the experiments was 25.6 °C. As a control, pure H_2O (100 μL) was irradiated with a 405 nm laser (210 mW) and only a slight temperature increase of 1.2 °C was recorded.

To further investigate the correlation between photothermal effect and the CDs-gluc concentration, additional experiments were conducted using sample dispersions with varying absorbance values at 405 nm. The results reported in Fig. 2E indicate temperature increases by about 42.6, 31.5, and 29.7 °C at absorbance ($\lambda = 405$ nm) values of 1.33, 0.26, and 0.13 unit, respectively. Representative thermographs of the photothermal experiments are shown in Fig. 2F. A high photothermal conversion efficiency (η) value of about 44.9 %, along with a photothermal time constant (τs) value of about 75.3 s, was calculated using the Roper's equation (Fig. S7). CDs-gluc exhibited photothermal conversion effect even after green-light irradiation (532 nm), Fig. S8 depicts the photothermal cycles of CDs-gluc water dispersion (5 mg/ml, $A_{532nm} = 0.25$) at different laser powers (100, 200, and 300 nm), with a photothermal conversion efficiency (η) value of about 42.67 %, and a photothermal time constant (τs) value of about 67.9 s. Additionally, photothermal effect was also observed upon light irradiation at 470 nm with a photothermal conversion efficiency (η) value of about 38 %, and a photothermal time constant (τs) value of about 103.7 s (Fig. S9).

2.3. CDs-gluc cytotoxicity

To ascertain the cytotoxicity of CDs-gluc, the proliferation of healthy CCD-841 cells (3,000 cells/well) was investigated in the presence of the nanostructures. Fig. 3 illustrates the percentage of cell growth after 24, 48, and 72 h of incubation withf 0.0, 0.01, 0.1, 1.0, and 10.0 μg of CDs-gluc. A control (CTRL) sample without nanostructures was used as a reference (cell proliferation 100 %). The data evidenced a very low cytotoxic effect of CDs-gluc, with cell mortality below 10 % in all experiments (Fig. 3). Statistical data from the cytotoxicity assays are provided in Table S1.

2.4. CDs-gluc cell internalization mediated by GLUT2

To ascertain whether the cellular internalization of CDs-gluc was indeed mediated by GLUT2 without any inherent limitations, particularly those of a steric nature, the Erickson's work on protein size characterization proved to be a crucial reference point [40]. The GLUT2 hydrodynamic diameter (Ds) was estimated to be approximately 5.06 nm from the relationship $Ds = 0.132\ M^{1/3}$, where M is the protein molecular weight (50–55 kDa). Therefore, CDs-gluc nanostructures with sizes of 1.1 ± 0.9 nm can effectively cross the cell membrane via GLUT2 transport.

2.4.1. GLUT2 transporter quantification

The expression of GLUT2 was investigated in three human cell lines from colon (cancer Caco-2 and HCT-116 cells and healthy CCD-841 cells) and three cell lines from breast (cancer MDA-MB-231 and MCF-7 cells and healthy 184A cells), by RT-qPCR experiments. The amount of mRNA (ng μL^{-1}) extracted from the six cell lines studied under different glucose conditions (Basal, Deprivation and Plus) is shown in Table S2.

GLUT2 mRNA levels were normalized to β-actin mRNA (used as an internal control), and results are expressed as fold change relative to β-actin. To avoid artifacts due to different compositions of growth media, all cells were grown in the same medium DMEM (see Material and Methods section). The relative GLUT2/β-actin mRNA ratio was measured under various concentrations of glucose in the medium and compared to elective reference culture media. In particular, the mRNA fold changes were measured in Basal condition (see Table S2 for the glucose amoun in the medium), Plus (glucose 10 mg L^{-1}) and Deprivation (glucose 0 mg L^{-1}) conditions.

The data shown in Fig. 4A demonstrate that the healthy colon CCD-841 cell line exhibits a modest increase in GLUT2 gene expression in response to glucose deprivation (1.25 ± 0.17 fold change). Conversely, under conditions of glucose abundance (Plus), the expression of this transport exhibits a pronounced weakening (0.14 ± 0.01 fold change) compared to the basal condition (1.0 fold change). Table S3 shows the RT-qPCR statistics for CCD-841 cells.

The colorectal adenocarcinoma CaCo-2 cell line showed a 1.71 ± 0.026 fold change under deprivation condition and 0.84 ± 0.11 fold change under Plus condition. Table S4 shows the RT-qPCR statistics for CaCo-2 cells.

The colon carcinoma HCT-116 cell line appears to be the most sensitive to change in glucose concentrations. When deprived of glucose, a net increase in GLUT2 gene expression was observed (35.47 ± 3.37 fold change), while under glucose-abundant conditions, GLUT2 gene expression decreased drastically (0.0047 ± 0.0003 fold change) in comparison to the basal reference. Table S5 shows the RT-qPCr statistics for HCT-116 cells.

Fig. 4A also illustrates the results of GLUT2 gene expression for the breast cell lines 184A1, MDA-MB-231 and MCF-7. Notably, under conditions of glucose deprivation and abundance, the healthy 184A1 cells

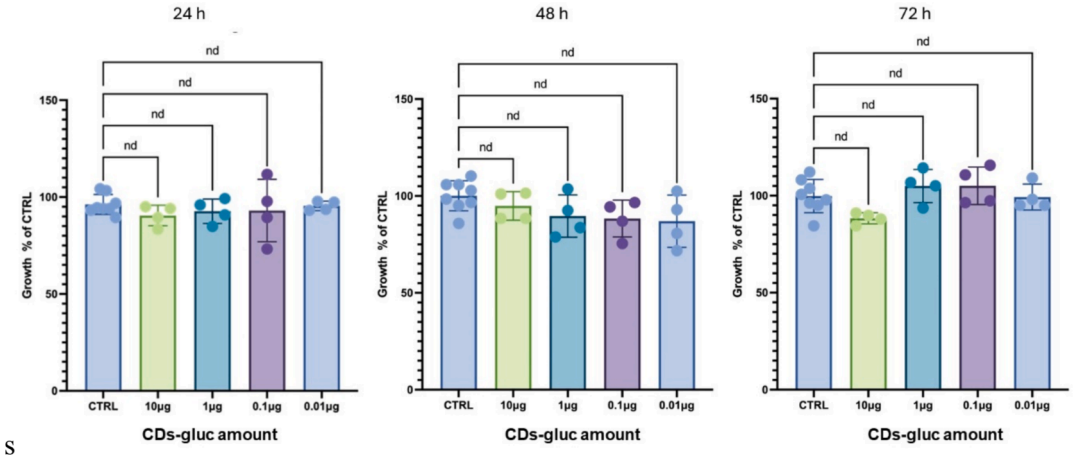

S

Fig. 3. CDs-gluc cytotoxicity as percentage of CCD-841 growth at various nanostructure concentrations (0.0, 0.01, 0.1, 1.0, and 10.0 μg) compared to the control after 24, 48, and 72 h of incubation. Data are represented as means ± standard deviation (SD).

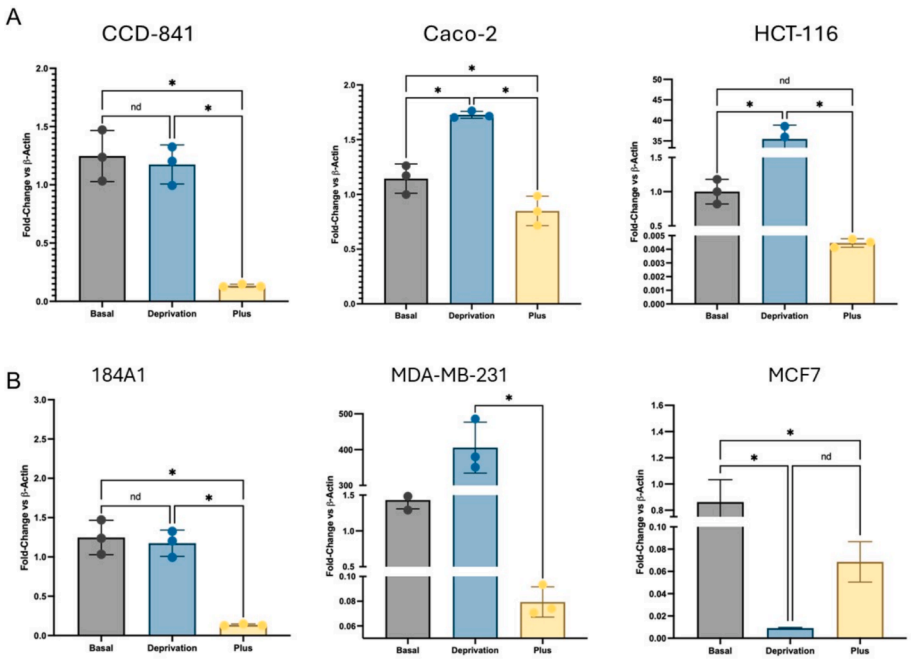

Fig. 4. GLUT2 gene expression of GLUT2/mRNA versus β-actin/mRNA as control for colon cell lines (CCD-841, Caco-2 and HCT-116) and breast cell lines (184A1, MDA-MB-231 and MCF-7) at different glucose amount: Basal (glucose amount equal to the specific medium used see Table S2, grey *bar*), Deprivation (0 g L^{-1}, blue *bar*) and Plus (10 g L^{-1}, yellow *bar*). The expressions are normalized using cells growth in the elective medium. Data are represented as means ± standard deviation (SD). Significantly different from Basal, * $p < 0.05$; ** $p < 0.01$, *** $p < 0.001$.

demonstrated a slight increase (1.23 ± 0.49 fold change) and decrease (0.072 ± 0.021 foldchange) in GLUT2 gene expression compared to the basal control. Conversely, in the tumor MDA-MB-231cell line, a markedly elevated level of GLUT2 expression was observed under glucose deprivation (405.4 ± 71.09 fold change) in comparison to the control condition. In glucose abundance, the fold change instead drops to approximately 0.079 ± 0.012 fold. Finally, MCF-7 cell line shows a decrease in both deprivation and plus conditions (0.0091 ± 0.0015 and 0.068 ± 0.019). Tables S6–S8 show the RT-qPCr statistics for 184A1, MDA-MB-231 and MCF-7 cells, respectively.

In summary, the RT-qPCR experiments showed different expression of the GLUT2 glucose transporter in response to varying glucose concentrations across the six cell lines investigated, emphasizing the complexity and specificity of cellular metabolic responses. The cancer HCT-116 and MDA-MB-231 cell lines exhibited the most sensitive GLUT2 gene expression to the glucose level.

The decrease of GLUT2 expression under glucose-abundant conditions (Plus) was indicative of a feedback mechanism to prevent excessive glucose uptake, which has been observed in other healthy tissues to maintain metabolic homeostasis [41]. While the increase of GLUT2 expression under glucose deprivation condition suggested that cells upregulate glucose transporters to enhance glucose uptake under low glucose conditions. In particular, the CaCo-2 colorectal adenocarcinoma cell line showed a slight GLUT2 expression change upon glucose amount variation, highlighting a potential characteristic of cancer cells to sustain glucose uptake irrespective of external glucose levels. This is consistent with the metabolic reprogramming often seen in cancer cells, known as the Warburg effect, where the cell relies heavily on glucose metabolism for energy production and biosynthesis, irrespective of glucose availability [42].

Conversely, the HCT-116 carcinoma line demonstrated a very pronounced sensitivity to glucose levels, with GLUT2 expression significantly decreasing under glucose-abundant conditions and markedly increasing under deprivation. This suggests a highly adaptive response of cancer cell to different glucose amounts. This adaptive mechanism has been documented in aggressive cancer phenotypes, which exhibit significant metabolic flexibility to survive and proliferate in varying environmental conditions [43]. The MDA-MB-231 tumor cell line exhibited a 400-fold increase in GLUT2 expression under glucose deprivation, highlighting an extreme adaptive mechanism to maximize glucose uptake under low glucose conditions. This extreme increase is consistent with findings in literature that aggressive breast cancer cells often show significant upregulation of glucose transporters to meet their heightened metabolic demands. In support of this, MCF-7 cell line shows low differences compared to the MDA-MB-231 because the MCF-7 line is normally considered less aggressive, being Estrogen Receptor Positive (ER+) [44]. Finally, in breast cell lines, the healthy 184A1 cells showed only modest changes in GLUT2 expression, indicating a stable regulation mechanism in non-cancerous cells. It is important to underline that all cell lines involved in this work showed a basal expression of GLUT2 comparable to the elective medium one, so the differences in Plus and Deprivation conditions can be correlated to the glucose concentration and not to the medium.

2.4.2. *CDs-gluc internalization assessments*

The quantity of internalized CDs-gluc under varying glucose concentrations was determined by measuring the CDs-gluc fluorescence signal (λ_{exc} = 350 nm; λ_{em} = 420 nm). In detail, 0.4 μg/μL of CDs-gluc was incubated in a 96-well plate, for 60 min, with different cell lines (Caco-2, HCT-116, MDA-MB-231, MCF-7, CCD-841 and 184A1, 10.000 cells/well), under both glucose-deprivation and glucose-plus conditions. Subsequently, fluorescence measurements were conducted, and the signal corrected for the autofluorescence of untreated control cells (Fig. 5). The experiments under basal condition were also performed as reference. The findings revealed that the uptake of CDs-glu is markedly influenced by the expression of GLUT2.

The data reported in Fig. 5 show a coherent correlation between GLUT2 expression and amount of CDs-gluc internalized. The largest amount of CDs-gluc were internalized by HCT-116 (33.54 ± 2.26 μg) and MDA-MB-231 (33.52 ± 6.06 μg) cells under glucose deprived condition, according to the higher GLUT2 gene expression reported in Fig. 4. While the CDs-gluc uptake dropwise to 9.25 ± 1.12 μg for HCT-16

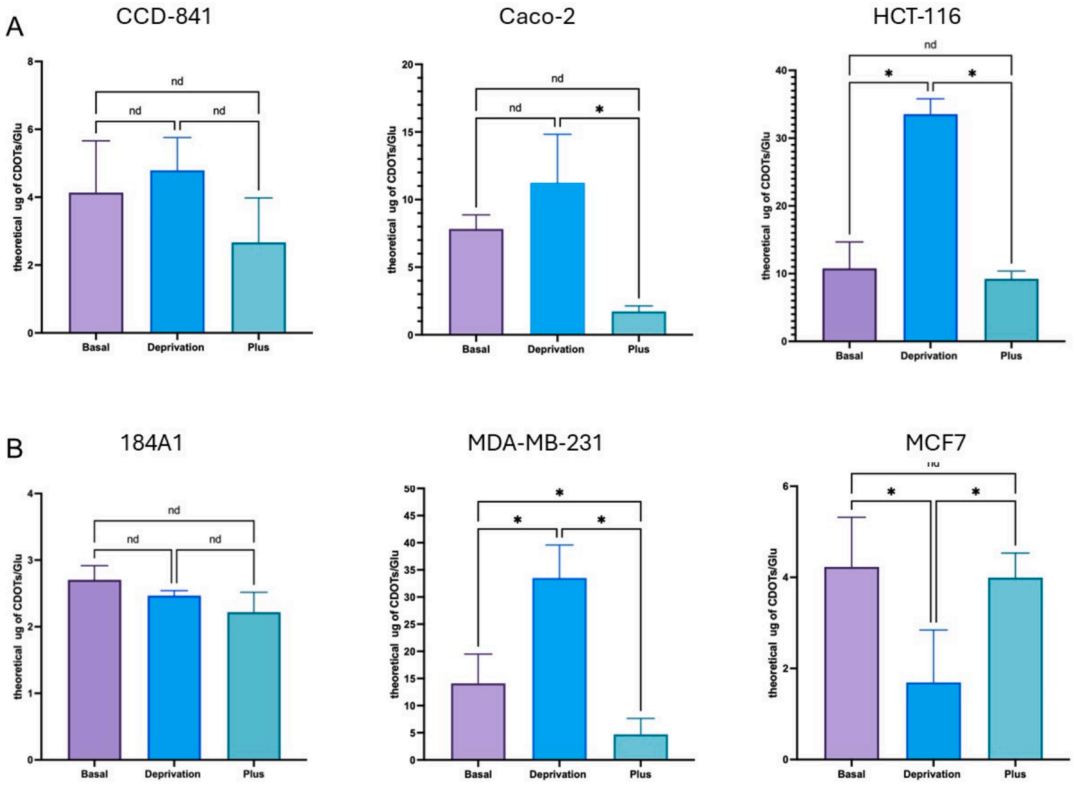

Fig. 5. CDs-gluc cell internalization mediated by GLUT2 membrane transport: for colon cell lines (CCD-841, Caco-2 and HCT-116) and breast cell lines (184A1, MDA-MB-231 *and* MCF-7) at different glucose amount: Basal reference control (violet line), Deprivation (0 g L^{-1}, azure line) and Plus (10 g L^{-1}, blue line). Data are represented as means ± standard deviation (SD). Significantly different from Basal, * $p < 0.05$; ** $p < 0.01$, *** $p < 0.001$.

and 4.71 ± 2.92 μg for MDA-MB-231 respectively under glucose-plus condition, where the lowest GLUT2 gene expression values were recorded. Under basal condition the amount of internalized CDs-gluc were 10.77 ± 3.90 μg for HCT-116 and 14.09 ± 5.40 μg for MDA-MB-231. MCF-7 cell line reported a GLUT2 fold change compared to β-actin of 0.86 ± 0.22 under Basal condition, 0.0091 ± 0.0015 under Deprivation and 0.068 ± 0.019 under Plus condition. The amount of CDs-gluc internalized agreed with this trend: under Basal condition is 4.22 ± 1.72 μg, under Deprivation 1.69 ± 1.38 μg and 3.99 ± 0.65 μg under Plus condition.

The experiments performed with the healthy cell 184A1 did not show significant differences in CDs-gluc internalization across different glucose amounts (2.467 ± 1.69 μg of CDs-gluc internalized under glucose-deprivation and about 2.219 ± 6.70 μg of CDs-gluc internalized under glucose-plus condition), according to the slight variations of GLUT2 gene expression (1.23 ± 0.49 change fold under glucose deprivation and 0.072 ± 0.021 change fold under glucose plus condition). Under basal condition the amount of internalized CDs-gluc was 2.7.04 ± 4.76 μg. The healthy CCD-841 cells did not show significant differences in CDs-gluc internalization under glucose deprivation condition (5.19 ± 1.11 μg) while a discrete decrease of internalized nanostructures was observed increasing the amount of glucose (2.66 ± 1.33 μg). Under basal condition the amount of internalized CDs-gluc was 4.13 ± 1.69 μg.

Conversely, CaCo-2 cells exhibited the lowest nanoparticle uptake, 1.73 ± 0.90 μg under glucose plus condition and the largest internalization of 11.24 ± 8.02 μg under glucose deprivation. According to the higher GLUT2 transport expression under glucose-deprived condition (1.71 ± 0.026 fold change) and lower GLUT2 transport expression under glucose-plus condition (0.84 ± 0.11 fold change). Under basal condition the amount of internalized CDs-gluc was 7.83 ± 2.33 μg. The raw data are reported in Tables S9–S14.

The evaluation of CDs-gluc internalization across different glucose concentrations revealed significant insights into the cellular uptake mechanisms and their dependence on metabolic states. The results demonstrated that glucose deprivation notably enhances CDs-gluc internalization in HCT-116 and MDA-MB-231 cells, with both cell lines exhibiting the highest uptake under these conditions, approximately 35 μg. This is consistent with previous studies indicating that cancer cells under metabolic stress often increase the uptake of different substances, potentially as a survival mechanism to exploit alternative metabolic pathways [45,46].

The observed variations in CDs-gluc uptake, particularly in HCT-116 and MDA-MB-231 cells, highlight the influence of glucose availability on cellular internalization mechanisms. The drastic increase in CDs-gluc uptake under glucose deprivation in these cancer cell lines can be related to their adaptive metabolic responses, which enhance endocytic activity to compensate for nutrient scarcity. This adaptability is a hallmark of cancer cells, supporting their survival and proliferation under adverse conditions.

The healthy cell lines, CCD-841 and 184A1, exhibited moderate CDs-gluc internalization, ranging from 2 μg to 4 μg in all glucose conditions, indicating a more consistent and regulated uptake mechanism. According to literature, this suggest that healthy cells maintain homeostasis and exhibit less variability in nanoparticle internalization compared to cancerous cells [47,48].

2.5. *Confocal microscopy and fluorescence correlation spectroscopy experiments*

Confocal imaging experiments confirmed the effective internalization of CDs-gluc into HCT-116 cells (20,000 cells/well) for all the conditions investigated, in accordance with the measurements of the GLUT2 gene expression. Fig. 6A illustrates representative bright-field (top) and confocal fluorescence (bottom) images of HCT116 cells without CDs-gluc (ctrl) and of cells exposed to 400 ng/μL of CDs-gluc after incubation at basal, deprivation and plus glucose condition. The images show

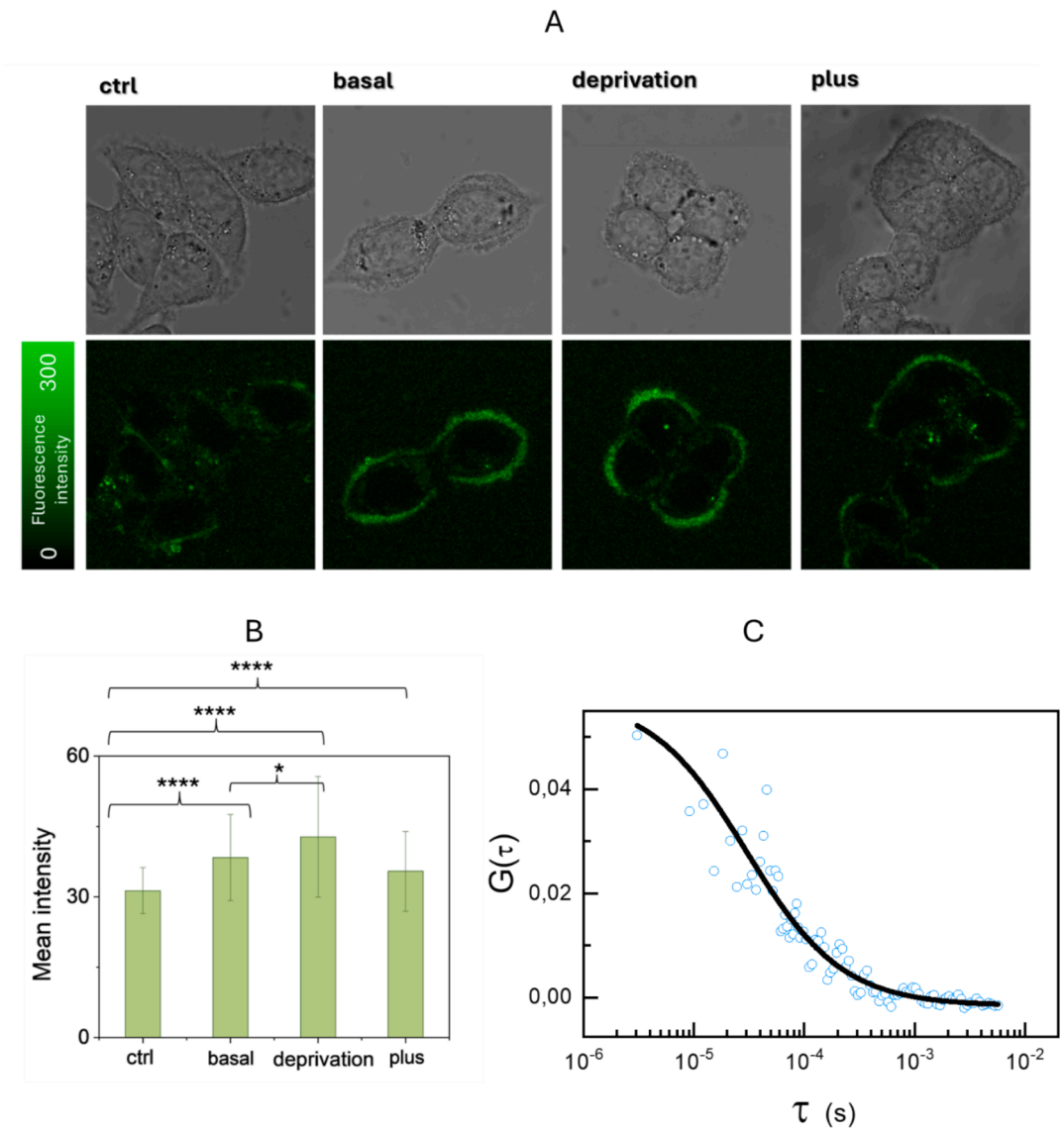

Fig. 6. CDs-gluc internalization and Fluorescence Correlation Spectroscopy experiments: A) Confocal imaging of HCT116 cells exposed to CDs-gluc. Representative bright-field (top) and confocal fluorescence (bottom) images of HCT116 cells not exposed to GLUT2 (ctrl) and exposed to CDs-gluc after incubation at basal, deprivation and plus glucose condition, B) Quantitative analysis of fluorescence intensity for the different conditions (p value < 0.001, ****; p value < 0.05, *).C) Fluorescence Correlation Spectroscopy (FCS) of CDs-gluc in solution. Diffusion analysis of GLUT2 in water solution. Representative autocorrelation function (ACF) obtained from FCS measurement. By fitting the average ACF to a proper model of diffusion, we extracted the diffusion coefficient value $D = (190 \pm 20)$ $\mu m^2/s$ (mean $\pm$ s.d., n = 3 independent measurements).

that after 1 hr incubation fluorescent CDs-gluc are located in the cytoplasmatic zone and around the cell membrane.

Compared to the control (31 ± 5 a.u, n = 48), a net increase in fluorescence signal was recorded in HCT-116 cells at the deprivation condition (43 ± 13 a.u., n = 109), in accordance with the previously detected higher gene expression (35.47 ± 3.37 fold change). Conversely, at the basal and plus conditions, slight increases in fluorescence signal compared to the ctrl were observed (basal condition 38 ± 9 a.u., n = 47, and plus condition 35 ± 8 a.u., n = 103), in accordance with the smaller gene expression at basal (1.0 ± 0.18 fold change) and plus (0.0044 ± 0.00031 fold change) conditions (Fig. 6B).

Fluorescence Correlation Spectroscopy (FCS) of CDs-gluc was performed in aqueous solution and at room temperature (Fig. 6C). FCS is based on the analysis of fluorescence intensity fluctuations arising from fluorescent nanoparticles freely diffusing through the confocal observation volume. The intensity fluctuations are analyzed through the intensity autocorrelation function (ACF) that enables the extraction of the diffusion coefficient of the nanoparticles. FCS showed that the CDs-gluc have a diffusion coefficient equal to D = 190 ± 20 $\mu m^2/s$ (mean ± s.d., n = 3). According to the Stokes–Einstein relationship, this D value corresponds to a hydrodynamic diameter of about 2.26 nm, consistent with the size obtained from AFM analysis.

2.6. *Targeted cell delivery of 5-fluorouracil entrapped in CDs-gluc (CDs-gluc/5Fu)*

To evaluate the potential of CDs-gluc as a nanocarrier for GLUT2-mediated cancer cell targeted drug delivery, 5-fluorouracil (5Fu), a known anticancer drug, was entrapped in the CDs-gluc nanostructures as reported in the experimental section. The effective 5FU entrapment in the CDs-gluc nanostructures was confirmed by optical absorption spectroscopy (Fig. 7A). In detail, the optical spectra of the CDs-gluc/5Fu adduct showed a sharp absorption band at around 266 nm for the 5Fu chromophore and a lower broad band at around 350–360 nm for the nπ*

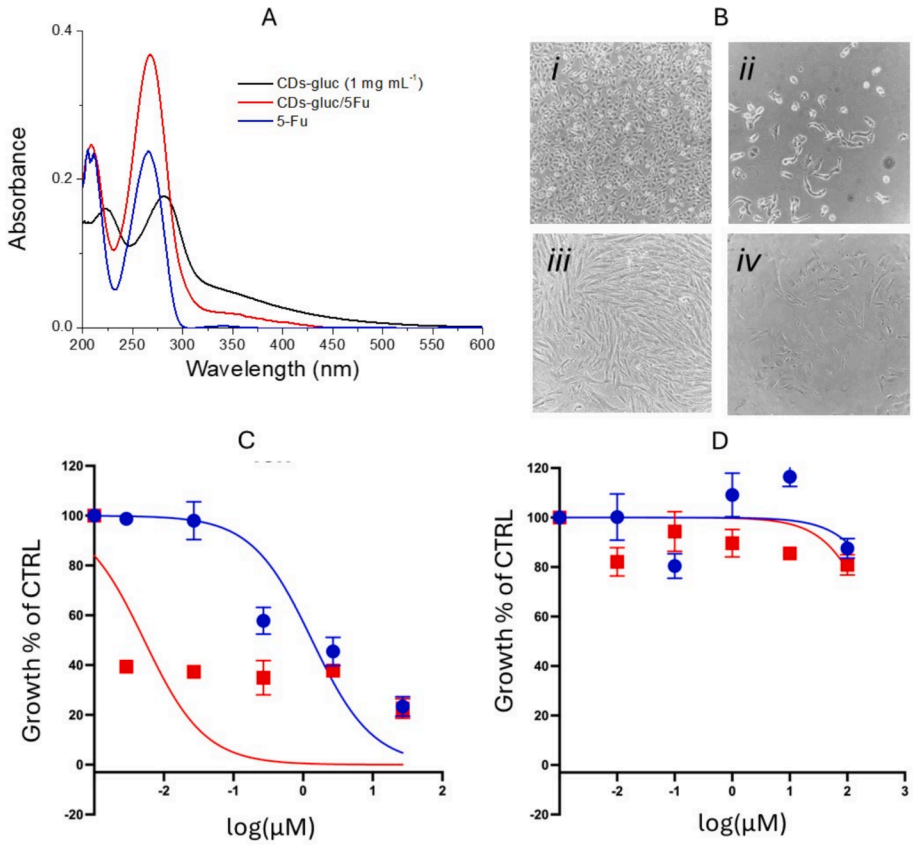

Fig. 7. CDs-gluc/5Fu optical absorption and cytotoxicity experiments: A) optical absorption spectra of CD-gluc/5FU, CD-gluc, and 5Fu dispersion in water, B) representative optical images (10X) for HCT-116 cells untreated (i) and treated (ii) with CD-gluc/5FU (100 ng/μL), and for CCD-841 cells untreated (iii) and treated (iv) with CD-gluc/5FU 100 ng/μL after 48 hrs of incubation. C) Dose–response curves of antiproliferative activities of HCT-116 (red square) and CCD-841 (blue circle) cells treated with different amount of CD-gluc/5FU, and D) with different amount of 5-FU after 48 hrs of incubation.

transition of the CDs-gluc (Fig. 7A red line). For comparison, the optical absorption spectrum for CDs-gluc dispersion (Fig. 7A black line) and 5Fu (Fig. 7A blue line) in water were also reported. The drug loading capacity value of 4.5 ± 0.8 % was calculated as described in the experimental section.

To assess the GLUT2-mediated cellular penetration of CD-gluc/4Fu, HCT-116 and CCD-841 cells were treated with different amounts of CDs-gluc/5Fu nanostructures (100, 10, 1, 0.1, 0.01 ng μL^{-1}, corresponding to a 5FU concentration of 26.9, 2.69, 0.269 μM and 26.9 and 2.69 nM). In vitro cell viability experiments were conducted under glucose deprivation conditions using 5FU alone (26.9, 2.69, 0.269 μM and 26.9 and 2.69 nM) as reference. Fig. 7B shows representative optical images of the untreated and treated (CD-gluc/5FU 100 ng μL^{-1}, corresponding to 26.9 μM of 5Fu) HCT-116 cells and CCD-841 cells after 48 h of incubation. According to the higher GLUT2 gene expression observed for HCT-116 cells under glucose deprivation conditions (Fig. 4C), a remarkable cytotoxicity effect was found for the cancer cells treated with different amount of CDs-gluc/5Fu (Fig. 7C red square). The comparison with the cytotoxicity observed for 5Fu alone (Fig. 7D red square) suggested a more effective cellular internalization of the drug vehiculated by the CDs-gluc nanostructures via GLUT2. A lower cytotoxicity was recorded for the CCD-841 healthy cells treated with CDs-gluc/5Fu (Fig. 7C blue circle), according to the lower GLUT2 gene expression observed under glucose deprivation mode in this cell line (Fig. 4A and 4D). Noteworthy, Fig. 7C shows a cell mortality above 63 % induced by a low 5-Fu amount (0.269 μM) for cancer cells and just 2 % for healthy cells treated with the same concentration of CDs-gluc/5Fu.

Noteworthy, the quantitative effect of CDs-gluc/5Fu on cell viability was confirmed by the IC50 values (Table S17), which were significantly lower in tumor HCT-116 cells (0.00522 μg/mL) than healthy CCD-841 cells (1.342 μg/mL). The IC50 values for HCT-116 and CCD-841 cells treated with 5Fu were 373.4 and 878.2 μM, respectively (Table S18).

Higher cell growth reduction and lower IC50 values for cancer cells with higher GLUT2 expression (glucose deprivation condition) clearly evidenced a GLUT2-mediated uptake of the CDs-glu/5Fu adduct and support the CDs-glu as promising nanocarriers for a more effective and faster tumor cell targeted drug delivery compared to free drug, requisite relevant for sparing healthy cells and reducing the amount of drug required for therapy.

2.7. *Cell Z-potential measurements*

The interaction of CDs-gluc with the HCT116 cell surface was corroborated by Z-potential analysis which provides information on the electric charge of the nanostructures and the cell membrane surface. The cell surface is usually negative due to carboxyl, phosphate or amino groups ionization and adsorption of ions from the medium. Proteins, phospholipids, teichoic acids, teichuronic acids and lipopolysaccharides, present in the cell membrane, also contribute to the net surface charge. In DEP-buffer HCT-116 cells and CDs-gluc showed a Z-potential of −19.6 ± 0.458 mV and −15.9 ± 1.07 mV, respectively. After 1 h of incubation of HCT-116 cells with CDs-gluc, a more negative cellular Z potential value (–22.3 ± 0.346 mV) was observed, resulting from the interaction of the CDs-gluc nanostructures with the cell surface (Fig. 8A). Our findings are consistent with existing literature, where the Z-potential has been used to study the interaction of nanomaterials with the bacteria membrane [49].

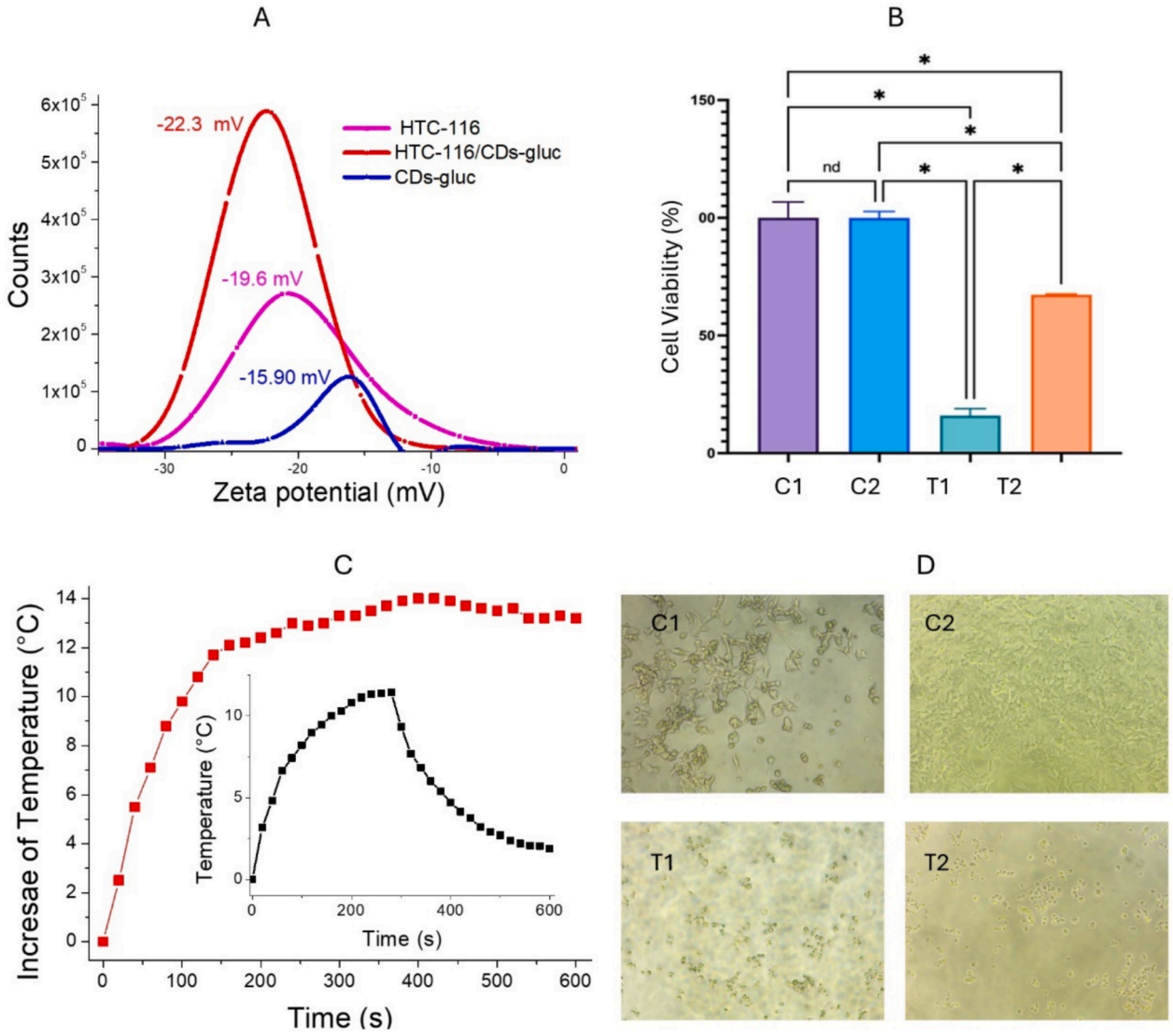

Fig. 8. A) Z-potential measurements for CDs-gluc water dispersion, HCT-116 cells suspension and HCT-116 cells/CDs-gluc after 1 h of incubation (all measurements were performed in DEP buffer and were replicated three times), B) Photothermal response effect of CDs-gluc on HCT-116 cells, MTT analysis of the cells treated with CDs-gluc without irradiation (C1), cells untreated but irradiated (*C*2), cells in glucose-deprivation condition treated with CDs-gluc and irradiation (T1) and cells in basal-condition treated with CDs-gluc and irradiation (T2). Bars represent means ± SEM of three independent experiments with $n = 3$. * $P < 0.05$; ** $P < 0.01$, *** $P < 0.001$, C) photothermal effects of CDs-gluc dispersion (2 μg μL^{-1}) upon laser 470 nm irradiation, and D) representative optical images (10X) of the samples investigated after treatment and 48hr of incubation.

2.8. In vitro light-triggered cell damage experiments induced by CDs-gluc

Due to the its peculiar optical properties, photo-irradiation of CDs-Glu with a properly excitation light could result in cell mortality. To evaluate the light-triggered cancer cell damage, HCT-116 cells in different glucose conditions (basal and deprivation) were treated with CDs-gluc (2 2μg μL^{-1}) and irradiated by a CW laser 470 nm for 4 min. The cell viability was investigated, by a standard MTT test after 48 h of incubation, on cells treated with CDs-gluc without irradiation (C1), cells untreated but irradiated (*C*2), cells in glucose-deprivation condition treated with CDs-gluc and irradiation (T1), and cells in basal-condition treated with CDs-gluc and irradiation (T2). The MTT assay showed no significant effect on the cell viability of the not irradiated samples (C1) and irradiated without CDs-gluc (*C*2). Interestingly, an effective cytotoxic effect was evident on irradiated cancer cells treated with CDs-gluc (T1 and T2). A prominent photoinduced cytotoxic effect was observed for the HCT-116 cells under deprivation condition (T1: cell mortality of about 85 %) where, as above reported, a higher amount of GLUT2 favours the Cdots-gluc internalization (Fig. 8). As a confirmation less cytotoxicity was observed under glucose-basal condition (T2: cell mortality about 35 %) because of a less expression of GLUT2 and consequently less nanostructures internalization.

Future studies should investigate the dynamics of GLUT expression over longer treatment periods, the potential for drug resistance, and the effects of combining CD-gluc/5Fu, photothermal effect and other therapeutic approaches. Integrating the concept of GLUT2 modulation into the design of nanotherapeutics, CD-gluc represents a promising advancement in the field of targeted cancer therapy. This approach not only enhances tumor selectivity but also provides a framework for exploiting cancer-specific metabolic vulnerabilities to improve therapeutic outcomes while minimizing adverse effects.

3. Conclusions

In this study, glucose-derived carbon dots (CDs-gluc) were synthesized via a single step by thermal treatment of glucose as the unique

precursor. The CDs-gluc nanostructures were characterized for structural, physicochemical, and optical properties. The as prepared carbon nanodots possess nanosize in the 0.2–2.0 nm range, good photoluminescence yield ($\phi_{PL} = 6$ %), and excellent photothermal conversion efficiency ($\eta = 42.7$ % at 532 nm). High biocompatibility, cell penetration properties, and excellent drug delivery capacity of 5-fluorouracil (LC = 4.5 ± 0.8 %) were also demonstrated. Cellular internalization of CDs-gluc was demonstrated to be mediated by the glucose transporter GLUT2. Indeed, the overexpression of GLUT2 induced under glucose starved conditions resulted in a net increase of CDs-gluc internalization in tumor cells. The different expression of GLUT2 at different glucose availability highlighted the disparate metabolic strategies deployed by healthy and cancerous cells in response to glucose. The increased sensitivity and adaptability of cancer cells to glucose deficiency, particularly for HCT-116 and MDA-MB-231 cell lines, mirror their reliance on altered glucose metabolism for survival and proliferation. These findings not only deepen the understanding of cancer cell metabolism but also suggest potential therapeutic targets for modulating the glucose transporter activity, that could have a significant impact on the metabolic processes of cancer cells. The demonstrated higher internalization of the glucose-derived carbon nanodots in glucose-deprived cancer cells indicates their potential for novel targeted anticancer therapeutic strategies, exploiting the metabolic vulnerabilities of cancer cells. In-vitro experiments confirmed the excellent photothermal cell damage activity of CDs-gluc upon light photoexcitation and the effective delivery of entrapped 5-fluorouracil to cancer cells, driven by a specific modulation of GLUT2 expression. Remarkable light-triggered cancer cell mortality of 85 % was observed for HCT-116 cancer cells treated with CDs-gluc (2 2μg μL^{-1}) and irradiated by a CW laser 470 nm for 4 min. The specific and excellent effect of CDs-gluc/5Fu on cancer cell damage was confirmed by lower IC50 recorded for HCT-116 cancer cell (IC50 = 0.00522 μg/mL) than for CCD-841 healthy cell (IC50 = 1.342 μg/mL). In conclusion, CDs-gluc nanostructures, which exhibit low cytotoxicity, glucose-mediated tumor cell targeting, photoluminescence, drug loading and delivery capacity, and photodynamic and photothermal conversion properties, are appealing and worthy of further investigation as a novel class of materials that exploiting the glucose avidity and GLUT2 overexpression of cancer cells can allow for a targeted anticancer treatment ranging from imaging to chemotherapic, photodynamic, and photothermal treatment. Future studies will focus on the application of CDs-gluc in combined multimodal therapy.

4. Experimental section

Chemicals and Instrumentation: All reagents including glucose were purchased by Merck and used as received. D(+) Glucose ≥ 99.5 % (Merck), Tetrachloroauric(III) acid trihydrate 99 % (Merck), methylene blue 99 % (Merck), Penicillin-Streptomycin (10,000 U/mL) Sterile-filtered (ThermoFisher – Ref. 15140122), DMEM, glucose-free Cell culture grade, (ThermoFisher – Ref. 11966025,), DEP Buffer (Made with Cell Culture Grade and Molecular Biology Grade reagents, then filtered wit 0.22 uM syringe filter), QuantiTect Probe RT-qPCR Kit, Molecular biology grade, (QIAGEN – Ref. 204345), Primers for RT-qPCR, desalting purification (IDT), MTT ≥ 97 % (TLC) (Merck), Milli-Q Water Ultrapure (18.2 MΩ·cm) (Merck Millipore system), Trypsin-EDTA solution (0.25 %), Cell culture grade, Thermo-Fisher. Optical absorption UV – vis spectra were acquired by a Perkin Elmer 365 spectrophotometer. A quartz cuvette with an optical length of 10 mm was used. ^{1}H NMR (400.13 MHz), ^{13}C NMR (100.61 MHz), and 2D-NMR spectra were acquired on a Bruker 400 MHz spectrometer at 297 K. Chemical shifts (δ, ppm) are relative to the residual proton solvent peak (D_2O, 4.72 ppm). Dynamic light scattering and Z-potential measurements were performed on a ZetaSizer NanoZS90 Malvern Instrument (U. K.), equipped with a 633 nm laser, at a scattering angle of 90°. The size of the particles was calculated from the diffusion coefficient by using the Stokes – Einstein equation.

CDs-gluc preparation: The CDs-gluc were prepared using the approach depicted in Scheme 1. Firstly, an amount of 500 mg of glucose was pyrolyzed for 45 min at 190 ± 3 °C, on a porcelain crucible, to obtain a carbon-nanodots material. The dark-reddish solid was washed with 2 mL of Milli-Q water to eliminate the excess of reagent and byproducts and finally sonicated for 5 min. The dispersion was separated by centrifugation (13,000 rpm for 10 min) and filtration (0.2 μm pore size), and then the red-yellowish supernatant of CDs-glu was purified by dialysis using Milli-Q water through a dialysis membrane (3.5 kDa cutoff, 2 mL volume) for 36 hrs. The purified sample was lyophilized at −80 °C. More than twenty preparation processes have been performed to confirm the reproducibility data.

CDs-gluc stability evaluation. The stability of CDs-gluc dispersion was evaluated in phosphate buffer saline overtime. The optical absorption of sample stored at room temperature in dark condition was measured every two days week, no significantly variation of absorbance value was observed overtime to indicate a good chemical stability (Fig. S10). Similarly, lyophilized samples investigated over 8 months do not showed significantly variation on optical absorption values.

Photoluminescence measurements: Photoluminescence (PL) spectra were obtained using a HORIBA spectrofluorometer. The emission was recorded at 90° to the direction of the exciting light with 3:3 nm slits width. The photoluminescence quantum yield (ϕ_{PL}) of the CDs-gluc dispersion in water (n = 1.33) was obtained using a solution of quinine sulfate (n = 1.36) as standard ($\phi_{PL} = 0.55$).

Photooxidation experiments: An aliquot of CDs-gluc (2 mL, 5 mg ml^{-1}) was mixed with methylene blue solution ($Abs_{665nm} = 0.5$) and irradiated under stirring with 300 nm 2 lamps (16 W). The experiments were replicated three times in aerated and deaerated conditions (15 min with argon gas). The optical absorption spectra were recorded at different irradiation time (10, 20, 30, 40, and 50 min). All experiments were replicated three times.

Photoreduction experiments (Au-nanostructures formation): To aliquots of 2 mL of CDs-gluc (0.5 mg/ml) in water was added a volume of 20 μL of $HAuCl_4$ (1.6×10^{-2} M), after degassing in argon for 15 min the sample was irradiated in a photoreactor equipped with 2 lamps (300 nm, 16 W) The formation of Au-nanostructures was investigated and confirmed by optical absorption UV–Vis spectra. All experiments were replicated three times.

Photothermal Measurements: The photothermal properties of CDs-gluc were investigated by irradiating a glass tube (3 mm in diameter) containing different amount of CDs-gluc dispersion in water. A volume of 100 μL of the CDs-gluc dispersion was irradiated with CW lasers with excitation wavelengths of 405 nm, 470 nm and 532 nm at different laser power for various minutes. A FLIR infrared thermal imaging camera was used to measure the temperature of the solution every 20 s, during the heating and cooling processes. All experiments were replicated three times.

Preparation of CDs-Gluc/5Fu: An amount of 5-fluorouracil (5Fu) 7.48 mg was dissolved in a volume of 2 mL of Cdots-Gluc water dispersion (1 mg mL^{-1}). The resulting mixture was stirred at room temperature in dark condition for 72 h. Then, the yellowish dispersion of CDs-Gluc/5Fu was purified by filtration through Amicon filter (M.W. cutoff of 3 kDa, 5,000 rpm for 20 min). This purification process included an additional washing step with 1 mL of water, followed by centrifugation at 5,000 rpm for 20 min. The adduct was lyophilized and stored before the use. The drug loading capacity percentage was calculated from the absorbance values of the drugs in the nanocarrier by applying the following formula:

$$LC(\%) = \frac{\text{mg drug in}}{\text{mg Cdots} + \text{mg drug in}}$$

Cell Z-potential measurements: An aliquot of 300 HCT-116 cells/μL solution (1 mL) was prepared and an amount of CDs-gluc (stock solution 1 mg/mL) was aliquoted to obtain a final concentration of 400 ng μL^{-1}.

The solutions were incubated for 1 and 2 hrs. After that, the samples were centrifuged at 200 g for 5 min, the supernatant was removed. The pellet was dispersed with 1 ml of DEP buffer and the Z-potential was measured in triplicate. For comparison, the Z-potential was measured for DEP buffer, cell alone and CDs-gluc dispersion (400 ng μL^{-1}).

RT-qPCR experiments: Gene expression measurements were performed by means of mRNA quantification using a LightCycler® 480 II instrument (Roche, Switzerland) using QuantiTect Probe PCR Kit (Ref. 204345, QIAGEN, Germany) and cDNA per well (25 ng total per well). Tables S15 and S16 show the primer sequences.

Real-time cycler conditions: Initial Activation Step, 15 min, 95 °C. 3-step cycling × 40 cycles: Denaturation, 15 s, 94 °C; Annealing, 30 s, 55 °C; Extension, 30 s, 72 °C (Fluorescence Acquisition in this step). As a negative control, a reaction in the absence of cDNA (no template control, NTC) was performed. The relative RNA expression level for each sample was calculated using the well-known 2−ΔΔCT method in which the threshold cycle (CT) value of the gene of interest is compared to the CT value of our selected internal control (β-actin). qRT-PCR amplifications were performed in triplicate.

Cytotoxicity evaluation (MTT assay): A MTT([3-(4,5-dimethylthiazol-2-yl)-2,5-diphenyltetrazolium bromide]) assay was performed as previously described [4] to test the CDs-gluc biocompatibility. CDs-glu nanoparticles (4 mg) were weighed and diluted in 40 μL of Nuclease Free Water, obtaining a stock solution of 0.1 mg/μL. Four serial dilutions were then created: 4 μg/μL, 400 ng/ μL, 40 ng/ μL, and 4 ng/ μL. Cells were treated with 10 μL of each solution. Untreated cells were used as controls. Microplates were incubated at 37 °C in a humidified atmosphere of 5 % CO_2, 95 % air for 24 hrs. The results were read on a multiwell scanning spectrophotometer BioTek Synergy H1 Multimode Reader (BioTek, USA), using a wavelength of 569 nm. Each value was an average of 4 wells. The statistically of changes in absorbance levels was assessed with the ANOVA assay. All statistical analysis were performed using GraphPad Prism 6.0 software. All experiments were replicated three times. Cytotoxicity experiments were performed also for cancer CaCo2 cells. Fig. S11 illustrates the percentage of cell growth after 24 hrs of incubation in the presence of 0.0, 0.02, 0.2, 2.0, and 20.0 μg of CDs-gluc. The control (CTRL) without nanostructures was used as a reference (cell proliferation 100 %). The data evidenced a very low cytotoxic effect of CDs-gluc with a dose-dependent cell growth reduction ranging from about 5.5 % to 13.8 % (Fig. S11). Table S19 shows the statistical data of the cytotoxicity experiments.

Different Glucose conditions: To test the change in the GLUT2 glucose transporter expression as glucose concentration changes, three different concentrations of glucose have been used: BASAL condition, where the concentration of glucose is equal to that of the elective medium of the cell line (CaCo-2 and MCF-7: 4,5 g/L, HCT-116 and MDA-MB231: 3 g/L, CCD-841 and 184A1: 1 g/L). Condition PLUS, where the glucose concentration is equal to 10 g/L, and finally the condition DEPRIVATION, corresponding to a glucose concentration equal to 0 g/L. The three conditions were prepared using glucose-free DMEM (Ref. 11966025, ThermoFisher Scientific, USA). In addition to these, an additional buffer formulated and tested for Electrorotation experiments, already reported by the research group [50] was used for zeta potential experiments. The glucose concentration of this DEP buffer was 0.1 g/L.

Time incubation: Once confluence was reached, each cell line was plated with 3 mL of medium of choice in a 6-well multiwell, with a population equivalent to approximately 100,000 cells/well. After 24 hrs, each multiwell was treated and in particular: in two wells the medium of choice was replaced with the BASAL condition, while in the remaining three wells it was replaced with the PLUS, DEPRIVATION and DEP BUFFER conditions. After 15 min of incubation in a humidified atmosphere of 5 % CO_2 and 95 % air, RNA was extracted from each cell line.

Confocal Microscopy Analysis: HCT-116 cells were plated (20.000 cells/well) on chambered coverslips (μ-Slide 8 Well Glass Bottom, Ibidi, Gräfelfing, MU, Germany) and allowed to grow overnight. The day after, cells were washed with PBS 1X, and then we reproduced control, basal, and plus conditions. Confocal fluorescence images were acquired on a Leica SP8 confocal microscope (Leica Microsystems, Wetzlar, Germany) with a 1.4NA 63 X oil immersion objective (HCPL APO CS2). The microscope has an incubation chamber to keep the cells at 37 °C and 5 % CO_2. The pinhole size was set to 1 Airy Unit. 1024 × 1024 pixel images were acquired using a line frequency of 700 Hz with 8 line average with a pixel size of 90 nm. An excitation wavelength of 405 nm was used, and the emission was detected in the band 450–650 nm via a hybrid detector. The transmitted light detector (TLD) channel was used to visualize the morphology of the cells. The fluorescence intensity was evaluated by selecting regions of interest (ROI) corresponding to single cells and extracting the average intensity value in the ROI. For each sample, a minimum of 50 cells were analyzed. All experiments were replicated three times.

Cell treatment with CDs-gluc/5FU: To evaluate the selective internalization of the CDs-gluc/5FU adduct, HCT-116 and CCD-841 cell lines were plated in a 96 multiwell and after 24 h treated with glucose deprivated medium for 1 h (to modulate GLUT2 expression) and then with CDs-gluc/5FU nanostructures (100, 10, 1, 0.1, 0.01 ng μL^{-1}, corresponding to a 5FU concentration of 26.9, 2.69, 0.269 μM and 26.9 and 2.69 nM) for additional one hour. As reference the experiments were also conducted using 5FU alone (26.9, 2.69, 0.269 μM and 26.9 and 2.69 nM) dissolved in the culture medium. After these two hours, the treated supernatant were removed and replaced with elective medium. The metabolic impact was evaluated with MTT assay after48 hours. All experiments were replicated three times.

5. Supporting information

Supporting Information is available from the Wiley Online Library or from the author.

CRediT authorship contribution statement

Nicolo Musso: Writing – original draft, Investigation. **Paolo Giuseppe Bonacci:** Investigation. **Grazia Maria Letizia Consoli:** Investigation. **Ludovica Maugeri:** Investigation. **Morena Terrana:** Investigation. **Luca Lanzanò:** Investigation. **Elisa Longo:** Investigation. **Gianpiero Buscarino:** Investigation. **Antonino Consoli:** Investigation. **Salvatore Petralia:** Writing – review & editing, Writing – original draft, Visualization, Validation, Supervision, Methodology, Investigation, Funding acquisition, Data curation, Conceptualization.

Declaration of competing interest

The authors declare that they have no known competing financial interests or personal relationships that could have appeared to influence the work reported in this paper.

Acknowledgements

This work has been funded by European Union (NextGeneration EU), through the MUR-PNRR project SAMOTHRACE (ECS00000022). We would like to thank the Bio-nanotech Research and Innovation Tower (BRIT) service center belonging to the University of Catania (Italy), for the use of its facility and instruments as well as for providing us a valuable technical assistance, and Dr. Riccardo Vinciguerra for his assistance during the setup of the experiments.

Appendix A. Supplementary data

Supplementary data to this article can be found online at https://doi.org/10.1016/j.jcis.2025.137873.

Data availability

The data are reported in supporting information file, more data are available on request.

References

[1] Z. Yang, T. Xu, H. Li, M. She, J. Chen, Z. Wang, S. Zhang, J. Li, Zero-Dimensional Carbon Nanomaterials for Fluorescent Sensing and Imaging, Chem. Rev. 123 (2023) 11047–11136, https://doi.org/10.1021/acs.chemrev.3c00186.

[2] J. Ren, H. Opoku, S. Tang, L. Edman, J. Wang, Carbon Dots: A Review with Focus on Sustainability, Adv. Sci. 11 (2024) 2405472, https://doi.org/10.1002/advs.202405472.

[3] G.M.L. Consoli, L. Maugeri, N. Musso, A. Gulino, L. D'Urso, P. Bonacci, G. Buscarino, G. Forte, S. Petralia, One-Pot Synthesis of Luminescent and Photothermal Carbon Boron-Nitride Quantum Dots Exhibiting Cell Damage Protective Effects, Adv. Healthcare Mater. 13 (2024) e2303692, https://doi.org/10.1002/adhm.202303692.

[4] G.M.L. Consoli, L. Maugeri, G. Forte, G. Buscarino, A. Gulino, L. Lanzano, P. Bonacci, N. Musso, S. Petralia, Red light-triggerable nanohybrids of graphene oxide, gold nanoparticles and thermo-responsive polymers for combined photothermia and drug release effects, J. Mater. Chem. B 12 (2024) 952–961, https://doi.org/10.1039/D3TB01863F.

[5] C. Zhao, J. Kang, Y. Li, Y. Wang, X. Tang, Z. Jiang, Carbon-Based Stimuli-Responsive Nanomaterials: Classification and Application, Cyborg Bionic Syst. 4 (2023) 0022, https://doi.org/10.34133/cbsystems.0022.

[6] Y. Wang, Y. Xu, J. Song, X. Liu, S. Liu, N. Yang, L. Wang, Y. Liu, Y. Zhao, W. Zhou, Y. Zhang, Tumor Cell-Targeting and Tumor Microenvironment-Responsive Nanoplatforms for the Multimodal Imaging-Guided Photodynamic/Photothermal/Chemodynamic Treatment of Cervical Cancer, Int. J. Nanomed. 13 (2024) 5837–5858, https://doi.org/10.2147/IJN.S466042.

[7] A. Ferlazzo, S. Bonforte, F. Florio, S. Petralia, L. Sorace, B. Muzzi, A. Caneschi, A. Gulino, Photochemical eco-friendly synthesis of photothermal and emissive copper nanoclusters in water: towards sustainable nanomaterials, Mater. Adv. 5 (2024) 8034–8041, https://doi.org/10.1039/d4ma00401a.

[8] E.W. Kavanagh, J.J. Green, Toward Gene Transfer Nanoparticles as Therapeutics, Adv. Healthc. Mater. 11 (2022) 2102145, https://doi.org/10.1002/adhm.202102145.

[9] L. Sun, H. Liu, Y. Ye, Y. Lei, R. Islam, S. Tan, R. Tong, Y.-B. Miao, L. Cai, Smart nanoparticles for cancer therapy, Sig. Transduct. Target Ther. 8 (2023) 418, https://doi.org/10.1038/s41392-023-01642-x.

[10] J. Wu, The Enhanced Permeability and Retention (EPR) Effect: The Significance of the Concept and Methods to Enhance Its Application, J. Pers. Med. 11 (2021) 771, https://doi.org/10.3390/jpm11080771.

[11] Y. Nakamura, A. Mochida, P.L. Choyke, H. Kobayashi, Nanodrug Delivery: Is the Enhanced Permeability and Retention Effect Sufficient for Curing Cancer? Bioconjug. Chem. 27 (2016) 2225–2238, https://doi.org/10.1021/acs.bioconjchem.6b00437.

[12] X.-J. Cai, Y.-Y. Xu, Nanomaterials in controlled drug release, Cytotechnology 63 (2011) 319–323, https://doi.org/10.1007/s10616-011-9366-5.

[13] N. Kamaly, B. Yameen, J. Wu, O.C. Farokhzad, Degradable Controlled-Release Polymers and Polymeric Nanoparticles: Mechanisms of Controlling Drug Release, Chem. Rev. 116 (2016) 2602–2663, https://doi.org/10.1021/acs.chemrev.5b00346.

[14] G. Forte, G. Consiglio, C. Satriano, L. Maugeri, S. Petralia, A nanosized photothermal responsive core-shell carbonized polymer dots based on poly(N-isopropylacrylamide) for light-triggered drug release, Coll. Surf. B: Biointerf. 217 (2022) 112628, https://doi.org/10.1016/j.colsurfb.2022.112628.

[15] L. Huang, Z. Li, Z. Xu, R. Yu, C. Ding, T. Sun, L. Kong, Z. Xia, C1GALT1 induces the carcinogenesis of thyroid cancer through regulation by miR-141-3p and GLUT1, Heliyon 10 (2024) e31778, https://doi.org/10.1016/j.heliyon.2024.e31778.

[16] K. Adekola, S.T. Rosen, M. Shanmugam, Glucose transporters in cancer metabolism, Curr. Opin Oncol. 24 (2012) 650–654, https://doi.org/10.1097/CCO.0b013e328356da72.

[17] L. Szablewski, Glucose transporters as markers of diagnosis and prognosis in cancer Diseases, Oncol. Rev. 16 (2022) 561, https://doi.org/10.4081/oncol.2022.561.

[18] Y. Xiang, Z. Xu, R. Qian, D. Wu, L. Lin, J. Shen, P. Zhu, F. Chen, C. Liu, Scutellarin Protects against Myocardial Ischemia-reperfusion Injury by Enhancing Aerobic Glycolysis through miR-34c-5p/ALDOA Axis, Int. J. Appl. Basic Med. Res. 14 (2024) 85–93, https://doi.org/10.4103/ijabmr.ijabmr_415_23.

[19] A. Zambrano, M. Molt, E. Uribe, M. Salas, Glut 1 in Cancer Cells and the Inhibitory Action of Resveratrol as A Potential Therapeutic Strategy, Int. J. Mol. Sci. 20 (2019) 3374, https://doi.org/10.3390/ijms20133374.

[20] Z. Chen, F. Han, Y. Du, H. Shi, W. Zhou, Hypoxic microenvironment in cancer: molecular mechanisms and therapeutic interventions, Sig. Transduct. Target Ther. 8 (2023) 1, https://doi.org/10.1038/s41392-023-01332-8.

[21] K.C. Carvalho, I.W. Cunha, R.M. Rocha, F.R. Ayala, M.M. Cajaíba, M.D. Begnami, R.S. Vilela, G.R. Paiva, R.G. Andrade, F.A. Soares, GLUT1 expression in malignant tumors and its use as an immunodiagnostic marker, Clinics (SaoPaulo) 66 (2011) 965–972, https://doi.org/10.1590/s1807-59322011000600008.

[22] J. Sieber-Frank, H.J. Stark, S. Kalteis, E.S. Prigge, R. Köhler, C. Andresen, T. Henkel, G. Casari, T. Schubert, W. Fischl, M. Li-Weber, P.H. Krammer, M. von Knebel Doeberitz, J. Kopitz, M. Kloor, A. Ahadova, Treatment resistance analysis reveals GLUT-1-mediated glucose uptake as a major target of synthetic rocaglates in cancer cells, Cancer Med. 10 (2021) 6807–6822, https://doi.org/10.1002/cam4.4212.

[23] Y. Zhang, Q. Li, Z. Huang, B. Li, E.C. Nice, C. Huang, L. Wei, B. Zou, Targeting Glucose Metabolism Enzymes in Cancer Treatment: Current and Emerging Strategies, Cancers (Basel) 14 (2022) 4568, https://doi.org/10.3390/cancers14194568.

[24] Z.E. Stine, Z.T. Schug, J.M. Salvino, C.V. Dang, Targeting cancer metabolism in the era of precision oncology, Nat. Rev. Drug Discov. 21 (2022) 141–162, https://doi.org/10.1038/s41573-021-00339-6.

[25] A.F. Abdel-Wahab, W. Mahmoud, R.M. Al-Harizy, Targeting glucose metabolism to suppress cancer progression: prospective of anti-glycolytic cancer therapy, Pharmacol. Res. 150 (2019) 104511, https://doi.org/10.1016/j.phrs.2019.104511.

[26] B. Thorens, GLUT2, glucose sensing and glucose homeostasis, Diabetologia 58 (2015) 221–232.

[27] A. Leturque, E. Brot-Laroche, M. Le Gall, GLUT2 mutations, translocation, and receptor function in diet sugar managing, Am. J. Phys. Endocrinol. Metab. 296 (2009) E985–E999, https://doi.org/10.1152/ajpendo.00004.2009.

[28] M. Pliszka, L. Szablewski, Glucose Transporters as a Target for Anticancer Therapy, Cancers 13 (2021) 4184, https://doi.org/10.3390/cancers13164184.

[29] C.-K. Chang, P.-F. Chiu, H.-Y. Yang, Y.-P. Juang, Y.-H. Lai, T.-S. Lin, L.-C. Hsu, L.-C.-H. Yu, P.-H. Liang, Targeting Colorectal Cancer with Conjugates of a Glucose Transporter Inhibitor and 5-Fluorouracil, J. Med. Chem. 64 (2021) 4450–4461, https://doi.org/10.1021/acs.jmedchem.0c00897.

[30] H.J. Heo, Y. Park, J.H. Lee, Y. Kim, E.K. Kim, G.H. Kim, Y. Yu, S.Y. Park, H.B. Seo, K. Pak, T.S. Goh, S. Park, S. Oh, W. Kwon, Y.H. Kim, Clinical big-data-based design of GLUT2-targeted carbon nanodots for accurate diagnosis of hepatocellular carcinoma, Nanoscale 14 (2022) 17053–17064, https://doi.org/10.1039/D2NR04238J.

[31] G.M.L. Consoli, M.L. Giuffrida, S. Zimbone, L. Ferreri, L. Maugeri, M. Palmieri, C. Satriano, G. Forte, S. Petralia, Green Light-Triggerable Chemo-Photothermal Activity of Cytarabine-Loaded Polymer Carbon Dots: Mechanism and Preliminary In Vitro Evaluation, ACS Appl. Mater. Interfaces 15 (2023) 5732–5743, https://doi.org/10.1021/acsami.2c22500.

[32] H. Liu, X. Zhong, Q. Pan, Y. Zhang, W. Deng, G. Zou, H. Hou, X. Ji, A review of carbon dots in synthesis strategy, Coord. Chem. Rev. 498 (2024) 215468, https://doi.org/10.1016/j.ccr.2023.215468.

[33] G.M.L. Consoli, M.L. Giuffrida, C. Satriano, T. Musumeci, G. Forte, S. Petralia, A novel facile one-pot synthesis of photothermally responsive carbon polymer dots as promising drug nanocarriers, Chem. Commun. 58 (2022) 3126–3129, https://doi.org/10.1039/D1CC06530K.

[34] A. Piasek, J. Pulit-Prociak, M. Zielina, M. Banach, Fluorescence of D-Glucose-Derived Carbon Dots: Effect of Process Parameters, J. Fluoresc. 34 (2023) 1693–1705, https://doi.org/10.1007/s10895-023-03392-z.

[35] M. Zhang, X. Fan, X. Du, Y. Ma, X. Wang, H. Huang, Y. Liu, Y. Li, Z. Kang, Chiral carbon dots from glucose by room temperature alkali-assisted synthesis for electrocatalytic oxidation of tryptophan enantiomers, Nano Res. 16 (2023) 8929–8936, https://doi.org/10.1007/s12274-023-5601-6.

[36] S. Cailotto, E. Amadio, M. Facchin, M. Selva, E. Pontoglio, F. Rizzolio, P. Riello, G. Toffoli, A. Benedetti, A. Perosa, Carbon Dots from Sugars and Ascorbic Acid: Role of the Precursors on Morphology, Properties, Toxicity, and Drug Uptake, ACS Med. Chem. Lett. 9 (2018) 832–837, https://doi.org/10.1021/acsmedchemlett.8b00240.

[37] J.M. Arroyave, R.E. Ambrusi, Y. Robein, M.E. Pronsato, G. Brizuela, M.S. Di Nezio, M.E. Centuriòn, Carbon dots structural characterization by solution-state NMR and UV–visible spectroscopy and DFT modeling, Appl. Surf. Sci. 564 (2021) 150195, https://doi.org/10.1016/j.apsusc.2021.150195.

[38] a) X. Fan, L. Huang, K.J.B. Sokorai, Factors affecting thermally induced furan formation, J. Agric. Food Chem. 56 (2008) 9490–9494, https://doi.org/10.1021/jf801612c;
b) J.M. Ames, Control of the Maillard reaction in food systems, Trends Food Sci. Technol. 1 (1990) 150–154, https://doi.org/10.1016/0924-2244(90)90113-D.

[39] D. Laroque, C. Inisan, C. Berger, E. Vouland, L. Dufossè, F. Guerard, Kinetic study on the Maillard reaction Consideration of Sugar Reactivity, Food Chem. 111 (2008) 1032–1042, https://doi.org/10.1016/j.foodchem.2008.05.033.

[40] H.P. Erickson, Size and shape of protein molecules at the nanometer level determined by sedimentation, gel filtration, and electron microscopy, Biol. Proced. Online 11 (2009) 32–51, https://doi.org/10.1007/s12575-009-9008-x.

[41] T. Okamoto, E.J. Park, E. Kawamoto, H. Usuda, K. Wada, A. Taguchi, M. Shimaoka, Endothelial connexin-integrin crosstalk in vascular inflammation, Biochim. Biophys. Acta Mol. basis Dis. 1867 (2021) 166168, https://doi.org/10.1016/j.bbadis.2021.166168.

[42] K. Hiesinger, K.M. Wagner, B.D. Hammock, E. Proschak, S.H. Hwang, Development of multitarget agents possessing soluble epoxide hydrolase inhibitory activity, Prostaglandins Other Lipid Mediat. 140 (2019) 31–39, https://doi.org/10.1016/j.prostaglandins.2018.12.003.

[43] U. Pfohl, A. Pflaume, M. Regenbrecht, S. Finkler, Q. Graf Adelmann, C. Reinhard, C.R.A. Regenbrecht, L. Wedeken, Precision Oncology Beyond Genomics: The Future Is Here—It Is Just Not Evenly Distributed, Cells 10 (2021) 928, https://doi.org/10.3390/cells10040928.

[44] R.M. Neve, K. Chin, J. Fridlyand, J. Yeh, F.L. Baehner, T. Fevr, L. Clark, N. Bayani, J.P. Coppe, F. Tong, T. Speed, P.T. Spellman, S. DeVries, A. Lapuk, N.J. Wang, W. L. Kuo, J.L. Stilwell, D. Pinkel, D.G. Albertson, F.M. Waldman, F. McCormick, R. B. Dickson, M.D. Johnson, M. Lippman, S. Ethier, A. Gazdar, J.W. Gray, A collection of breast cancer cell lines for the study of functionally distinct cancer

subtypes, Cancer Cell 10 (2006) 515–527, https://doi.org/10.1016/j.ccr.2006.10.008.
[45] N.N. Pavlova, C.B. Thompson, The Emerging Hallmarks of Cancer Metabolism, Cell Metab. 23 (2016) 27–47, https://doi.org/10.1016/j.cmet.2015.12.006.
[46] M.G. Vander Heiden, L.C. Cantley, C.B. Thompson, Understanding the Warburg effect: the metabolic requirements of cell proliferation, Science 324 (2009) 1029–1033, https://doi.org/10.1126/science.1160809.
[47] B.D. Chithrani, A.A. Ghazani, W.C.W. Chan, Determining the Size and Shape Dependence of Gold Nanoparticle Uptake into Mammalian Cells, Nano Lett. 6 (2006) 662–668, https://doi.org/10.1021/nl052396o.
[48] A. Albanese, P.S. Tang, W.C.W. Chan, The effect of nanoparticle size, shape, and surface chemistry on biological systems, Ann. Rev. Biomed. Eng. 14 (2012) 1–16, https://doi.org/10.1146/annurev-bioeng-071811-150124.
[49] M.S. Kuyukina, M.V. Makarova, O.N. Pistsova, G.G. Glebov, M.A. Osipenko, I. B. Ivshina, Exposure to metal nanoparticles changes zeta potentials of Rhodococcus cells, Heliyon 8 (2022) e11632, https://doi.org/10.1016/j.heliyon.2022.e11632.
[50] P.G. Bonacci, G. Caruso, G. Scandura, C. Pandino, A. Romano, G.I. Russo, R. Pethig, M. Camarda, N. Musso, Impact of buffer composition on biochemical, morphological and mechanical parameters: A tare before dielectrophoretic cell separation and isolation, Transl. Oncol. 28 (2023) 101599, https://doi.org/10.1016/j.tranon.2022.101599.

Salvatore Petralia received the Ph.D. degree in chemistry from the University of Catania (UniCT), Catania, Italy, in 2003. Since 2023, he has been an Associate Professor of Chemistry with the University of Catania. From 2004 to 2020, he was a Technology Development Sect. Manager with STMicroelectronics Italy, covering research and development positions. His research activities cover multidisciplinary aspects of chemistry, nanostructured materials, sensing and biosensing. In this field, he has coauthored 145 peer-reviewed scientific publications, one chapter of book and is a co-inventor of 12 applications patents.

Nicolo Musso is Professor at the "Kore" University of Enna and Head of the Laboratory for Eukaryotic and Host Pahogen Interactions at the University of Catania. Graduating with honors in Physical Activity Sciences, he holds a Ph.D. in Neurobiology and a National Scientific Qualification in General Biochemistry. His career spans over 15 years of research in genomics, proteomics, and molecular diagnostics. He specializes in advanced molecular biology techniques, including NGS, qRT-PCR, and dielectrophoresis, applied to the study of pathogens and tumor biomarkers. His work includes projects on antimicrobial resistance, genetic characterization of solid tumors, and the development of nanoparticles for cancer therapies. He is coauthor of numerous publications in international journals, he has been awarded for innovative contributions in molecular diagnostics, such as SNP analysis in SARS-CoV-2 variants. He has collaborated with academic and industrial entities, including QIAGEN and STLab.